Atmospheric
Chemistry
and Physics
Discussions

Exploring the sensitivity of atmospheric nitrate concentrations to nitric acid uptake rate using the Met Office's Unified Model

Anthony C. Jones[1], Adrian Hill[1], Samuel Remy[2], N. Luke Abraham[3,4], Mohit Dalvi[1], Catherine Hardacre[1], Alan J. Hewitt[1], Ben Johnson[1], Jane P. Mulcahy[1], and Steven T. Turnock[1]

[1] Met Office, Fitzroy Road, Exeter, EX1 3PB, UK
[2] HYGEOS, Lille, France
[3] National Centre for Atmospheric Science, U.K.
[4] Department of Chemistry, University of Cambridge, Lensfield Road, Cambridge, CB2 1EW, U.K.

Correspondence to: Anthony C. Jones (anthony.jones@metoffice.gov.uk)

Abstract.

Ammonium nitrate is a major aerosol constituent over many land regions and contributes to air pollution episodes, ecosystem destruction, regional haze, and aerosol-induced climate forcing. Many climate models that represent ammonium nitrate assume that the ammonium-sulphate-nitrate chemistry reaches thermodynamic equilibrium instantaneously without considering kinetic limitations on condensation rates. The Met Office's Unified Model (UM) is employed to investigate the sensitivity of ammonium nitrate concentrations to the nitric acid uptake coefficient (γ) in a newly-developed nitrate scheme in which first order condensation theory is utilised to limit the rate at which thermodynamic equilibrium is attained. Two values of γ representing fast ($\gamma = 0.193$) and slow ($\gamma = 0.001$) uptake rates are tested in 20-year global UM integrations. The global burden of nitrate associated with ammonium in the 'fast' simulation (0.11 Tg[N]) is twice as great as in the 'slow' simulation (0.05 Tg[N]), while the top-of-the-atmosphere radiative impact of representing nitrate is -0.19 Wm^{-2} in the 'fast' simulation and -0.07 Wm^{-2} in the 'slow' simulation. In general, the 'fast' simulation exhibits better spatial correlation with observed nitrate concentrations while the 'slow' simulation better resolves the magnitude of concentrations. Local near-surface nitrate concentrations are found to be highly correlated with seasonal ammonia emissions suggesting that ammonia is the predominant limiting factor controlling nitrate prevalence. This study highlights the high sensitivity of ammonium nitrate concentrations to nitric acid uptake rates and provides a mechanism for reducing nitrate concentration biases in climate model simulations. The new UM nitrate scheme represents a step-change in aerosol modelling capability in the UK across weather and climate timescales.

1 Introduction

Air pollution poses a significant hazard to human-health and to the environment world-wide. In 2016, 90 % of the global population were exposed to pollutant concentrations in excess of World Health Organisation (WHO) defined safe levels, resulting in ~7 million premature deaths (WHO, 2020). Specific human-health conditions arising from air pollution exposure

include lung cancer and cardiopulmonary disease, and deleterious impacts also extend to ecosystems (e.g. eutrophication, loss of biodiversity, acid deposition), building and infrastructure erosion, and impaired atmospheric visibility and regional haze (Kucera and Fitz, 1995; Monks et $al.$, 2009; Lovett et $al.,$ 2009; Xu et $al.$, 2019). Solid or liquid particulate matter (PM) is a significant component of air pollution and particles with diameters less than 2.5 µm (i.e. $PM_{2.5}$) are particularly harmful to

35   human health. Lelieveld et $al.$ (2015) estimate $PM_{2.5}$ related global mortality to be 3.3 million deaths yr^{-1} in 2010, far greater than the second deadliest air pollutant, ozone (O_3, 142 thousand deaths yr^{-1}). Sources of air pollution differ with region; in North Africa and the Middle East, the predominant source is naturally emitted dust; in Europe, agricultural activity; and in South East Asia, residential energy production (Lelieveld et $al.$, 2015).

40   Secondary inorganic ammonium (NH_4), sulphate (SO_4), and nitrate (NO_3) aerosol form a major part of $PM_{2.5}$ composition in the Northern Hemisphere (Jiminez et $al.$, 2009). Ammonium is predominantly emitted as ammonia (NH_3) gas by agricultural sources such as mineral fertilizer application and volatilization of livestock manure; biomass burning and from ocean emission (Bauer et $al.$, 2016). NH_3 emissions from agriculture have dramatically increased since the discovery of the Haber-Bosch process for extracting reactive nitrogen from its stable atmospheric form (N_2) in the early 20th Century. The

45   corresponding NH_3-based fertilizer revolution led to significantly enhanced global food production and a population explosion from 2 billion to 7 billion people (Smith et $al.$, 2020). However, reactive nitrogen deposition from fertiliser usage is now 20-fold higher than it was before the industrial revolution (Xu et $al.$, 2019). NO_3 is formed from atmospheric nitric acid (HNO_3), itself an oxidation product of nitrogen oxides (NO_x = NO + NO_2). NO_x is primarily emitted from anthropogenic fossil fuel burning (21-28 Tg N yr^{-1}) but has natural sources including soil emissions, biomass burning and

50   lightning (12-35 Tg N yr^{-1}) (Seinfeld and Pandis, 1998; Vinken et $al.$, 2014). NO_x exacerbates air pollution via two pathways – by NO_3 aerosol production and by net O_3 production in the presence of sunlight and volatile organic compounds (VOCs) (Crutzen, 1970). SO_4 is the oxidation product of sulphur dioxide (SO_2), which is primarily emitted by anthropogenic processes such as fossil fuel combustion, petroleum refining, and metal smelting (Zhong et $al.$, 2020). Natural SO_2 sources include volcanic degassing and the oxidation of reduced natural sulphurous compounds such as dimethyl sulphide (DMS)

55   (Carn et $al.$, 2017). Global anthropogenic SO_2 emissions have steadily declined from a peak of ~70 Tg S yr^{-1} in the 1980s to ~52 Tg S yr^{-1} in 2014 owing to clean air regulation instigated to mitigate adverse SO_2 impacts such as acid rain (Mcduffie et $al.$, 2020; Zhong et $al.$, 2020). Global NO_x emissions peaked in 2010 at ~40 Tg N yr^{-1}, with emissions growth from 1990-2010 driven by rapid industrialisation in Asia and intensified international shipping, but have decreased by 7 % over the 2010s owing primarily to traffic emission control measures in China (Mcduffie et $al.$, 2020).

60

In the troposphere, NO_x is involved in a complex diurnal photochemical cycle involving VOCs and O_3. The dominant NO_x removal mechanism during daytime is via oxidation by hydroxyl (OH) radicals to form HNO_3 (Seinfeld and Pandis, 1998). At night-time, NO_2 is unable to photolyze and the dominant NO_x removal mechanism is via reaction with O_3 to produce the NO_3 radical; which further reacts with NO_2 to form dinitrogen pentoxide (N_2O_5); which heterogeneously reacts with water (H_2O)

65   to produce HNO_3 (Atkinson, 2000). HNO_3 is abundantly soluble and rapidly dissolves in water droplets or is neutralised by NH_3 to form aerosol. SO_2 is oxidised in the aqueous phase by dissolved oxidants such as O_3 and hydrogen peroxide (H_2O_2), and in the gas phase by OH, to form non-volatile H_2SO_4 (Seinfeld and Pandis, 1998). H_2SO_4 and HNO_3 react with NH_3 to produce ammonium sulphate (($NH_4)_2 \cdot SO_4$) and semi-volatile ammonium nitrate ($NH_4 \cdot NO_3$) aerosol respectively, with H_2SO_4 neutralisation taking precedence owing to the lower vapor pressure of H_2SO_4 over HNO_3 (Hauglustaine *et al.*, 2014). In a

70   slower process, HNO_3 also condenses irreversibly onto existing dust and sea-salt aerosols, forming calcium nitrate ($Ca \cdot (NO_3)_2$) and sodium nitrate ($Na \cdot NO_3$) salts respectively (Li and Shao, 2009). Owing to the prevalence of anthropogenic NO_x and NH_3 sources, particulate NO_3 is a major component of urban air pollution. For example, in Europe NO_3 constitutes 17 % of urban $PM_{2.5}$ aerosol by mass (Putaud *et al.*, 2004), while $NH_4 \cdot NO_3$ can comprise 75 % of $PM_{2.5}$ in air pollution events in Salt Lake City (Womack *et al.*, 2019).

75

Nitrate aerosol has an enigmatic history within the climate modelling community owing to the complexity of modelling HNO_3 neutralisation by NH_3 and the semi-volatility of $NH_4 \cdot NO_3$ aerosol. In the inorganic aerosol system, gaseous and particulate equilibria are reached at different rates due to evolving temperature and acidity constraints, and the variability in gaseous uptake with particle size (Myhre *et al.*, 2006; Benduhn *et al.*, 2016). Although complex dynamical and 'hybrid dynamical'

80   schemes that fully or partially resolve the chemistry of inorganic aerosol exist (e.g. Jacobson, 1997; Feng and Penner, 2007; Zaveri *et al.*, 2007; Benduhn *et al.*, 2016; Xu and Penner, 2012), they remain computationally expensive – owing to the numerical stiffness of the inorganic system – when compared to schemes that assume thermodynamic equilibrium is reached instantaneously (Nenes *et al.*, 1998). Most of the current crop of nitrate-resolving global climate models (GCMs) and some regional climate models (RCMs) assume the instantaneous thermodynamic equilibrium approximation (Liao *et al.*, 2003;

85   Myhre *et al.*, 2006; Bauer *et al.*, 2007; Bellouin *et al.*, 2011; Hauglustaine *et al.*, 2014; Paulot *et al.*, 2016; Bian *et al.*, 2017; Remy *et al.*, 2019). Dynamical models have the advantage of capturing natural phenomena where the inorganic aqueous system is outside of (or slow to reach) equilibrium, for instance in low gas concentrations, low temperatures, high Relative Humidities (RH), and for condensation onto coarse particles (Wexler and Seinfeld, 1990; Benduhn *et al.*, 2016). Thermodynamic equilibrium models typically overestimate the fraction of NO_3 in the coarse mode, for example, in one study NO_3 associated

90   with fine mode $NH_4 \cdot NO_3$ was underestimated by 25 % compared to a hybrid-dynamical model (Feng and Penner, 2007). However, the additional computational expense of using dynamical approaches has motivated the climate modelling community to seek pragmatic solutions to represent NH_4 and NO_3 aerosol in GCMs and RCMs.

GCM simulations suggest that the present-day direct radiative forcing from NO_3 (global mean $\approx$ -0.1 Wm^{-2}) amounts to a

95   quarter of the SO_4 forcing on a global-mean basis (Myhre *et al.*, 2006; Bauer *et al.*, 2007; Bellouin *et al.*, 2011; Hauglustaine *et al.*, 2014). NO_3 aerosol burdens are widely projected to increase over the 21st century as a result of stricter SO_2 emissions regulations, which would reduce the SO_4 available for neutralisation and concomitantly liberate NH_4 for $NH_4 \cdot NO_3$ formation (Bauer *et al.*, 2007; Bellouin *et al.*, 2011). Consequently, NO_3 may become the dominant aerosol species in terms of radiative

and urban air pollution impact by the end of the century, depending on future emissions of SO_2, NH_3 and NO_x (Hauglustaine
100   *et al.*, 2014). Such NO_3 concentration enhancements may be effectively mitigated on a regional basis by judicious regulation
targeting anthropogenic NH_3 and/or NO_x emissions (Bauer *et al.*, 2016). However, climate models disagree as to whether near-
surface NO_3 concentrations will increase or decrease in future climate, and on the correct partitioning between NO_3 in the fine
mode (associated with NH_4) and coarse mode (associated with dust and sea-salt) (Bian *et al.*, 2017). Many of the uncertainties
in NH_4 and NO_3 projections emanate from different treatments of the HNO_3 and NH_3 gases in models, with Bian *et al.* (2017)
105   highlighting wet deposition as a particularly sensitive process. Additionally, the vertical distributions of HNO_3 and NH_3 are
poorly constrained by observations which adds to uncertainty in NH_4 and NO_3 projections (Paulot *et al.*, 2016).

The emerging conclusion from observations and from the burgeoning literature on nitrate modelling is that ammonium nitrate
poses an increasingly significant health hazard through urban air pollution (e.g. DEFRA, 2012) and via deposition to nitrogen-
110   saturated ecosystems (Li *et al.*, 2016); and potentially could become a major climate forcing agent as SO_4 concentrations wane
(Hauglustaine *et al.*, 2014). The impetus for explicitly representing NH_4 and NO_3 in GCMs is clear, even by using simple
thermodynamic equilibrium approaches which bypass temporal nuances in the gas-particulate partitioning. The Met Office
Unified Model (UM) has previously incorporated a thermodynamic-equilibrium ammonium nitrate scheme in the CMIP5-
generation climate model Hadley Centre Global Environment Model version 2 (HadGEM2-ES) (Bellouin *et al.*, 2011). This
115   nitrate scheme – developed within the single-moment Coupled Large-scale Aerosol Simulator for Studies in Climate
(CLASSIC) aerosol framework (Bellouin *et al.*, 2007) – continues to be utilised for online air quality forecasts across the UK
in the operational Air Quality Unified Model (AQUM) (Savage *et al.*, 2013). However, the CMIP6-generation state-of-the-art
United Kingdom Earth System Model version 1 (UKESM1) which incorporates the Global Atmosphere model vn7.1 (GA7.1)
(Walters *et al.*, 2019) replaced the single-moment CLASSIC aerosol scheme with the double-moment Global Model of Aerosol
120   Processes modal (GLOMAP-mode) scheme which currently omits ammonium nitrate (Mann *et al.*, 2010; Mulcahy *et al.*,
2020). Mulcahy *et al.* (2020) attributed a negative bias in aerosol optical depth and mass burden over northern hemisphere
continents in UKESM1 to the missing NH_4 and NO_3. The hybrid-dynamical nitrate scheme developed by Benduhn *et al.* (2016)
in the standalone GLOMAP-mode model is yet to successfully transition to the UM. This has provided the Met Office with
fresh impetus to develop a simplified thermodynamic equilibrium nitrate scheme within the GLOMAP-mode framework for
125   interim use in the UM and possible implementation in future generations of UKESM, in order to fill the NH_4 and NO_3 shaped
void. The nitrate scheme may garner further utility if AQUM or its successor transitions to utilising the GLOMAP-mode
aerosol scheme rather than CLASSIC (Hemmings and Savage, 2018).

In this paper we describe the development and testing of a simple thermodynamic equilibrium nitrate scheme in the UM and
130   explore the sensitivity of the scheme to a key parameter that is poorly constrained by observations – the HNO_3 uptake
coefficient on aerosol surfaces (γ). Specifically, most models assume that $NH_4 \cdot NO_3$ concentrations reach thermodynamic
equilibrium instantaneously without considering kinetic limitations on the condensation of HNO_3 or NH_3 onto existing aerosol

particles, as is considered here. The UM nitrate scheme reported here comprises fine NH_4 and NO_3 aerosol in the Aitken, accumulation, and coarse soluble modes and coarse NO_3 representing NO_3 aerosol associated with dust and sea-salt in the

135 accumulation and coarse soluble modes. The scheme was originally developed by Hauglustaine *et al.* (2014) for use in the LMDZ-INCA climate model, then adapted for ECMWF's version of GLOMAP-mode by Remy *et al.* (2019), following which it was kindly provided to the Met Office for adaptation to the UM. In Section 2.1, we describe the configuration of the UM used to test the new nitrate scheme. In Section 2.2, we describe the thermodynamic equilibrium nitrate model in detail. In Section 2.3 we describe the simulations performed in this study. In Section 3, we evaluate the model using surface and satellite

140 observations and investigate the sensitivity of the model to perturbations to a key parameter – the HNO_3 uptake coefficient (γ) – in a manner analogous to Bauer *et al.* (2004). In Section 4, we discuss the utility of the nitrate scheme and provide a roadmap for future development and integration within UKESM.

2 Methods

2.1 The Met Office Unified Model (UM)

145 The nitrate scheme was originally developed using the UM with the science configurations Global Atmosphere vn7.1 (GA7.1) and Global Land vn7.0 (GL7.0) (Walters *et al,* 2019). Although the UM can be run at various resolutions, the resolution used here is the climate configuration N96L85, i.e. 1.875° longitude by 1.25° latitude with 85 vertical levels up to a model lid at 80 km, with 50 levels below 18 km altitude, and a model timestep of 20 mins (Walters *et al*, 2019). The UM's dynamical core, Even Newer Dynamics for General atmospheric modelling of the environment (ENDGame), is a semi-implicit and semi-

150 Lagrangian solver for the non-hydrostatic deep-atmosphere equations of motion (Wood *et al.*, 2014). Mass conservation of moist tracers is achieved using the Optimised Conservative Filter scheme (Zerroukat and Allen, 2015). Atmospheric radiative transfer is modelled assuming the two-stream approximation, with 6 wavebands in the shortwave spectrum and 9 wavebands in the longwave spectrum (Manners *et al*., 2015). Large-scale cloud is modelled with the Prognostic Cloud fraction and Prognostic Condensate (PC2) scheme (Wilson *et al.*, 2008) and cloud microphysics uses the single-moment scheme based on

155 Wilson and Ballard (1999) with extensive modifications. Full details of GA7.1/GL7.0 are provided in Walters *et al*. (2019) and Mulcahy *et al*. (2018).

In the model configuration used here, GA7.1 includes the United Kingdom Aerosol and Chemistry (UKCA) model which simulates atmospheric composition in the Earth System, with UKCA chemistry called once per model hour in N96L85,

160 although emissions are evaluated every model timestep (Archibald *et al*., 2020). UKCA is coupled to the GLOMAP-mode aerosol scheme, permitting a holistic and prognostic treatment of aerosol and chemical processes over the entire atmosphere (Mann *et al*., 2010; Mulcahy *et al*., 2020). The coupled UKCA and GLOMAP-mode model is widely referred to as UKCA-mode. The Met Office's Hadley Centre Global Climate version 3.1 (HadGEM3-GC3.1) model – the physical basis of UKESM1 – uses a simplified UKCA chemistry configuration with important offline oxidants (O_3, OH, NO_3, HO_2) provided as monthly

165   mean climatologies (Walters *et al.*, 2019; Mulcahy *et al.*, 2020). This is of insufficient complexity for ammonium nitrate aerosol, given the importance of missing gases (i.e. HNO_3, NH_3 and precursors) and chemical reactions. Instead the combined Stratospheric-Tropospheric version 1.0 (StratTrop 1.0) chemistry scheme, which is included in UKESM1 (Sellar *et al.*, 2019) and described in detail by Archibald *et al.* (2020), is utilised here. Although not mentioned in Archibald *et al.* (2020), gaseous ammonia (NH_3) is a passive tracer in StratTrop1.0, while gaseous nitric acid (HNO_3) is the product of various atmospheric

170   chemical reactions (see Table S1 in the Supplement). StratTrop1.0 simulates the chemical cycles of O_x, HO_x, NO_x, and halogenic compounds; the oxidation of various organic compounds; and heterogenous chemistry on Polar Stratospheric Cloud (PSCs), Nitric Acid Trihydrate (NAT) and tropospheric aerosols, with 84 species and 291 chemical reactions. Further details of the nitrogen chemistry in StratTrop1.0 is provided in Section 2.2. Interactive photolysis in UKCA is modelled with the Fast-JX scheme, which covers the wavelength range 177-750 nm (Telford *et al.*, 2013). Gaseous wet deposition follows the effective

175   Henry's law approximation described in Giannakopous *et al.* (1999) while dry deposition is treated with a resistance type model (O'Connor *et al.*, 2014). Gaseous dissolution in cloud droplets is modelled using the effective Henry's law framework, with UKCA uniformly assuming a fixed cloud water pH of 5.0. Values required to calculate the effective Henry's law coefficients are specified as $K_H(298K) = 2.1\times10^5$, 1.23, and 1×10^6 for HNO_3, SO_2 and NH_3 respectively, and $-\Delta H/R = 8700$, 3020, and 0 K^{-1} for HNO_3, SO_2 and NH_3 respectively (Archibald *et al.*, 2020). The values for NH_3 are comparable to AeroCom

180   phase III values given in Table 5 in Bian *et al.* (2017).

GLOMAP-mode is a prognostic double-moment aerosol scheme that carries aerosol mass and number concentrations in 4 soluble lognormal modes spanning sub-micron to super-micron sizes (nucleation, Aitken, accumulation, and coarse), as well an insoluble Aitken mode (see Table 1) (Mann *et al.*, 2010; Mulcahy *et al.*, 2020). The variable size distribution allows the

185   median dry radius to evolve within prescribed size brackets, while the lognormal standard deviation or 'mode width' is held fixed. GA7.1's default GLOMAP-mode configuration includes the aerosols sulphate (SO_4), black carbon (BC), organic matter (OM), and sea-salt (SS), with species in each mode treated as an internal mixture. Mineral dust is represented in GA7.1 by the CLASSIC 6 bin scheme described by Woodward *et al.* (2001). Aerosol processes in GLOMAP-mode include binary homogeneous SO_4 nucleation, mode-merging, cloud processing, condensational uptake of H_2SO_4 gas and secondary organic

190   vapour from UKCA, and coagulation within and between modes. Aerosol water content is simulated prognostically using the Zdanovskii-Stokes-Robinson (ZSR) method, allowing for a more accurate representation of aerosol-cloud interactions and aerosol radiative impact than in CLASSIC. The direct aerosol radiative effect is modelled using UKCA-Radaer, which utilises pre-determined look-up tables of Mie extinction parameters based on aerosol size and composition (Bellouin *et al.*, 2013). Cloud condensation nuclei are converted to cloud droplets using UKCA-Activate which is based on the Abdul-Razzak and

195   Ghan (2000) parameterization, while autoconversion of cloud droplets to rainwater follows Khairoutdinov and Kogan (2000) (Boutle *at al.*, 2014; West *et al.*, 2014; Mulcahy *et al.*, 2018). Aerosol removal processes treated by UKCA-mode include dry deposition and sedimentation, in-cloud scavenging by the autoconversion of cloud to rainwater; beneath cloud scavenging by rain and snow impaction; and convective plume scavenging (Mann *et al.*, 2010, Mulcahy *et al.*, 2020).

Aerosol Mode	Geometric mean diameter $\bar{D}$ (nm)	σ_g	Species
Nucleation soluble	1 – 10	1.59	SO$_4$, OM
Aitken soluble	10 – 100	1.59	SO$_4$, BC, OM, NH$_4$, NO$_3$
Accumulation soluble	100 – 1000	1.4	SO$_4$, BC, OM, SS, NH$_4$, NO$_3$, hetNO$_3$
Coarse soluble	> 1000	2.0	SO$_4$, BC, OM, SS, NH$_4$, NO$_3$, hetNO$_3$
Aitken insoluble	10 - 100	1.59	BC, OM

200

Table 1: Properties of the aerosol size distribution in the nitrate UKCA-mode setup including the size range of the modes, the geometric standard deviation, and the permitted aerosol species in each mode. Species include sulphate (SO$_4$), black carbon (BC), organic matter (OM), sea-salt (SS) and the newly added ammonium (NH$_4$), nitrate (NO$_3$) and coarse nitrate (hetNO$_3$). Adapted from Table 1 in Mulcahy *et al*. (2020).

205

2.2 Nitrate model

In addition to the standard aerosols in GA7.1 - SO$_4$, BC, OM, and SS - ammonium (NH$_4$), nitrate (NO$_3$) and coarse nitrate (herein denoted hetNO$_3$ for convenience) are added to a new UKCA-mode setup which comprises 28 aerosol tracers in total (Table 1). NH$_4$ and NO$_3$ mass is emitted into the Aitken and accumulation soluble modes and may be transferred to the coarse

210 soluble mode via aerosol processing, while hetNO$_3$ is limited to the accumulation and coarse soluble modes. Nitrate chemistry is evaluated once per model timestep within the UKCA emissions-control routine. The nitrate model closely follows Hauglustaine *et al*. (2014) and Remy *et al*. (2019) with subtle yet important differences. An exhaustive step-by-step methodology is provided in the Supplement (Sections S1 and S2) and outlined below.

2.2.1 Ammonium nitrate production

215 Fine mode ammonium nitrate production is evaluated before the condensation of HNO$_3$ onto coarse aerosols (e.g. sea-salt and dust) because smaller particles generally reach thermodynamic equilibrium faster (Hauglustaine *et al*., 2014; Benduhn *et al*., 2016). Firstly, the sulphate neutralisation state (Γ_{SO_4}) is determined from the total moles of ammonia ($T_A = \{NH_3\} + \{NH_4^+\}$) and total moles of sulphate ($T_S = \{SO_4\}$) using Eq. 1 (Metzger *et al*., 2002).

220
$$\Gamma_{SO_4} = \begin{cases} 2 & 2\,T_S < T_A & 2NH_3 + H_2SO_4 \;\rightarrow\; (NH_4)_2SO_4 \\ 1.5 & T_S < T_A < 2\,T_S & 3NH_3 + 2H_2SO_4 \;\rightarrow\; (NH_4)_3H(SO_4)_2 \\ 1 & T_A < T_S & NH_3 + H_2SO_4 \;\rightarrow\; (NH_4)HSO_4 \end{cases}$$
[1]

The moles of ammonia available for neutralisation of HNO_3 following the irreversible production of ammonium sulphate is then $T_A^* = T_A - \Gamma_{SO_4} T_S$. If all free ammonia is consumed by the neutralisation of SO_4 ($T_A^* = 0$) then no new nitrate is formed. However, if ammonia is available ($T_A^* > 0$) then the equilibrium constant (K_p) of the ammonia-nitrate system (Eq. 2) is

225   determined using the parameterisation of Mozurkewich (1993) (see Section S1 in the Supplement). In this formulation, K_p is solely a function of temperature and Deliquescence Relative Humidity (DRH), with DRH following the parameterisation of Seinfeld and Pandis (1998).

$$HNO_3 + NH_3 \overset{K_p}{\leftrightarrow} NH_4NO_3 \qquad [2]$$

230

The equilibrium concentration of ammonium nitrate is then calculated using the formulation from Seinfeld and Pandis (1998). Letting T_N denote the total molar concentration of nitrate ($T_N = \{HNO_3\} + \{NO_3^-\}$), if $T_A^* T_N > K_p$ then the molar concentration of ammonium nitrate aerosol at equilibrium is calculated using Eq. 3. Else if free ammonia or nitrate concentrations are limited such that $T_A^* T_N \leq K_p$ or $T_A^* = 0$ then all existing ammonium nitrate aerosol evaporates and the corresponding mass is

235   transferred to the gas phase HNO_3 and NH_3.

$$\{NH_4NO_3\}_{eq} = \frac{1}{2}\left[T_A^* + T_N - \sqrt{(T_A^* + T_N)^2 - 4(T_N T_A^* - K_p)}\right] \qquad [3]$$

The ammonia-nitrate system may not reach equilibrium within a standard GCM timestep owing to transport limitations

240   between the gas and aerosol phases (Wexler and Seinfeld, 1990). The time taken to reach equilibrium depends on ambient temperature and RH, and the aerosol size and uptake coefficient (γ), where the uptake coefficient is defined as the number of gas molecules condensing on a particle divided by the number impacting onto the particle surface. Ackerman *et al*. (1995) find that equilibration time (τ) may range from ~2 minutes for particles with diameters of 0.1 µm to ~1 hour for diameters of 0.5 µm, depending on the uptake rate. Remy *et al*. (2019) assumed a globally uniform equilibration time of $\tau = 2$ minutes in their

245   nitrate model. Here the uptake rate k_{HNO3} is determined for each aerosol mode online (Aitken, accumulation, and coarse soluble) using the first order uptake theory of Schwartz (1986) and by applying the Fuchs and Sutugin (1970) correction factors for molecular effects and for limitations in interfacial mass transport (Eqs 4-7).

$$D_g = \frac{3}{8A_c \rho_a d_a^2}\left[\frac{m_a R_a T}{2\pi} \times \frac{m_a + m_{HNO3}}{m_{HNO3}}\right]^{\frac{1}{2}} \qquad [4]$$

250

$$\lambda = \frac{3D_g}{\upsilon} = \frac{3D_g}{\sqrt{\frac{8R_a T}{\pi m_{HNO3}}}} \qquad [5]$$

$$K_n = \frac{2\lambda}{D} \qquad [6]$$

$$k_{HNO3} = \frac{2\pi D D_g}{1 + \frac{4K_n}{3\gamma} \times \left(1 - \frac{0.47\gamma}{1 + K_n}\right)} \qquad [7]$$

Equations 4-7 determine the molecular diffusivity coefficient (D_g, m^{2}s^{-1}), the mean free path (λ, m), the Knudsen number (K_n),

255   and the modal condensation or uptake rate (k_{HNO3}, m^{3}s^{-1}) respectively. Constants in the algorithm include the Avogadro

constant $A_c = 6.022 \times 10^{23}$ mol^{-1}, the gas constant of dry air $R_a = 8.314$ J mol^{-1} K^{-1}, the molar mass of dry air $m_a = 0.029$

kg mol^{-1}, the molar mass of HNO$_3$ $m_{HNO3} = 0.063$ kg mol^{-1}, the molecular diameter of dry air molecules $d_a = 4.5 \times 10^{-10}$ m,

and the reactive uptake coefficient (γ) for HNO$_3$. Variables in Eqs 4-7 include the air temperature T (K) and air density ρ_a (kg

m^{-3}). In Eq. 5, υ is the mean molecular speed (m s^{-1}). The total equilibration time τ (s) may then be related to the inverse of

260   product of the uptake rate for one particle k_{HNO3} and the aerosol number concentration N using Eq. 8. Note that ammonium

nitrate production is limited to the Aitken and accumulation modes in this study, which is reflected in the formulation of τ.

$$\tau = \frac{1}{N_{ait}k_{HNO3,ait} + N_{acc}k_{HNO3,acc}} \qquad [8]$$

265   Rather than assume instantaneous thermodynamic equilibrium in the ammonia-nitrate system, the model assumes an

exponential decay of the gas phase towards equilibrium using the equilibration time τ (see Section S1.4 in the Supplement).

This approach has also been used by Ackerman *et al.* (1995), Makar *et al.* (1998), and Remy *et al.* (2019). Figure S3 in the

Supplement shows the results of applying the above algorithm for τ (with γ set to 0.193 following Feng and Penner (2007)) to

monthly mean aerosol and meteorology output from example UM integrations. Over many land regions, τ is approximately 2

270   mins near the surface and increases to ~15 mins at a model level height of 3000 m. Therefore, assuming a constant value of

$\tau = 2$ mins, as assumed by Remy *et al.* (2019), may significantly overestimate the rate which the ammonia-nitrate system

approaches equilibrium, particularly at higher altitudes and over maritime regions. For example, in a 20-minute timestep the

ammonia-nitrate system would move 99.995 % of the way from initial conditions towards equilibrium with $\tau = 2$ mins

assuming exponential decay, but only 86 % of the way with $\tau = 10$ mins and 33 % of the way with $\tau = 50$ mins.

275

For standard atmospheric conditions ($D_g = 10^{-5}$ m^{2}s^{-1} and $\upsilon = 300$ ms^{-1}), k_{HNO3} scales approximately linearly with the

reactive uptake coefficient γ, for γ from 0.001 to 0.2 and for particle diameters between $D = 0.1$ μm and $D = 5$ μm (Figure

S2 in the Supplement). The uptake rate increases on a particle-by-particle basis with diameter, for example, ranging from 0.2

s^{-1} for $D = 0.1$ μm to 5 s^{-1} for $D = 0.5$ μm when $\gamma = 0.1$ and when k_{HNO3} is normalised by $N = 10^{12}$ m^{-3}. However,

280   atmospheric Aitken mode number concentrations generally exceed accumulation mode concentrations, particularly over

Atmospheric
Chemistry
and Physics
Discussions
Open Access
EGU

populous land regions and increasingly with altitude. In example UM integrations, the ratio of accumulation to Aitken uptake ($N_{acc}k_{HNO3,acc}/N_{ait}k_{HNO3,ait}$) decreases on a global-mean basis from 8 at the surface to 1.4 at a model level height of 3000 m, but is effectively unity at the surface over key NH_3 and NO_x emitting regions such as the US, Europe and South Asia (Figure S4 in the Supplement).

285

Uptake rates (k_{HNO3}, Eq. 7) are determined for the Aitken and accumulation modes by using the modal geometric-mean dry diameters for D in Eqs 4-7, which are first corrected for hygroscopic growth using the RH-dependent parameterisation of Gerber *et al.* (1985). This simplified 'modal' approach differs from Hauglustaine *et al.* (2014) who divide aerosol size modes into sub-bins. If $T_A^* T_N > K_p$ then mass is transferred from the gaseous reactants NH_3 and HNO_3 to NH_4 and NO_3 in the Aitken

290 and accumulation soluble modes using the above algorithm. Else if $T_A^* T_N \leq K_p$ then NH_4 and NO_3 dissociate and all NH_4 and NO_3 mass in the Aitken to coarse soluble modes is instantaneously transferred to the gas phase. Ammonium nitrate chemistry solely involves condensation and evaporation (Makar *et al.*, 1998; Benduhn *et al.*, 2016); thus, aerosol number concentrations are not altered explicitly by nitrate chemistry in our model but may change indirectly due to altered coagulation and mode-merging rates arising from the additional aerosol mass. This approach differs from Hauglustaine *et al.* (2014) and Remy *et al.*

295 (2019) who assume that new particles are nucleated by the production of ammonium nitrate.

2.2.2 Coarse nitrate production

Following $NH_4 \cdot NO_3$ production and the associated update to HNO_3 concentrations, the first order uptake parameterisation described by Eqs 4-7 is further employed to model the irreversible uptake of HNO_3 on sea-salt and dust to produce $NaNO_3$ (Eq. 9) and $Ca(NO_3)_2$ (Eq. 10) respectively (Liao *et al.*, 2003; Hauglustaine *et al.*, 2014).

300

$$HNO_3 + NaCl \rightarrow NaNO_3 + HCl \qquad [9]$$
$$2HNO_3 + CaCO_3 \rightarrow Ca(NO_3)_2 + H_2CO_3 \qquad [10]$$
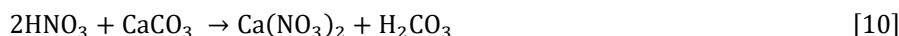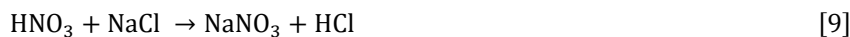
The methodology is mostly unchanged from Hauglustaine *et al.* (2014) and Remy *et al.* (2019), with only subtle adaptations

305 needed to integrate the scheme within UKCA-mode. As in Hauglustaine *et al.* (2014), the HNO_3 uptake coefficients (γ) for dust and sea-salt are RH-dependent variables based on measurements from Fairlie *et al.* (2010) for dust and Sander *et al.* (2011) for sea-salt. Additionally, dust is assumed to uniformly constitute 5 % Ca^{2+} by mass, which differs from the approach in Remy *et al.* (2019) who used a spatially hetereogeneous Ca^{2+} fraction. Dust alkalinity is titrated by uptake of HNO_3 until the dust pH is neutralised whereupon HNO_3 stops condensing, while no such limitation is applied for sea-salt.

310

As for the first order uptake parameterisation for ammonium nitrate (Section 2.2.1) and in Remy *et al.* (2019), rather than explicitly integrating the uptake rate over the aerosol size distribution, k_{HNO3} is calculated individually for sea-salt in the

accumulation and coarse modes using the modal geometric-mean diameters for D in Eqs 4-7, and individually for each CLASSIC dust bin using fixed geometric mean diameters (see Section S2 in the Supplement). Sea-salt number concentrations

315 for the two modes are inversely determined from the sea-salt mass concentrations and the modal geometric-mean dry diameters, which implicitly assumes that sea-salt is externally mixed with other UKCA-mode aerosols. Dust particle number concentrations are determined from prognostic dust mass concentrations and fixed size distributions for each bin. Mapping between CLASSIC's 6 dust bins and UKCA-mode's 2 size modes follows the approach currently used to map dust emissions between CLASSIC and UKCA-mode, with Bin 2 and half of Bin 3 mapped to the accumulation mode and the other half of

320 Bin 3 and Bins 4, 5 and 6 mapped to the coarse mode. The dust and sea-salt uptake rates (k) multiplied by the equivalent particle number concentrations (N) are then used to determine tendencies to mass concentrations of coarse NO_3 aerosol (hetNO_3), sea-salt (SS), and HNO_3 gas (Eqs 11-13). The constants in Eqs 11-13 include the molar mass of $Ca(NO_3)_2$ $m_{Ca(NO3)2} = 0.164$ kg mol^{-1}, the molar mass of $NaNO_3$ $m_{NaNO3} = 0.084$ kg mol^{-1}, the molar mass of HNO_3 $m_{HNO3} = 0.063$ kg mol^{-1}, and the molar mass of $NaCl$ $m_{NaCl} = 0.05844$ kg mol^{-1}.

325

$$\frac{\Delta[\text{het}NO_3]}{\Delta t} = \left(\left(Nk_{du,ACC} + Nk_{du,COA} \right) \times \frac{m_{Ca(NO3)2}}{m_{HNO3}} + \left(Nk_{SS,ACC} + Nk_{SS,COA} \right) \times \frac{m_{NaNO3}}{m_{HNO3}} \right) \times [HNO_3] \qquad [11]$$

$$\frac{\Delta[HNO_3]}{\Delta t} = - \left(2 \times \left(Nk_{du,ACC} + Nk_{du,COA} \right) + \left(Nk_{SS,ACC} + Nk_{SS,COA} \right) \right) \times [HNO_3] \qquad [12]$$

$$\frac{\Delta[SS]}{\Delta t} = - \left(Nk_{SS,ACC} + Nk_{SS,COA} \right) \times \frac{m_{NaCl}}{m_{HNO3}} \times [HNO_3] \qquad [13]$$

330 **2.2.3 Technical UM modifications**

UKCA-Radaer calculates 3D aerosol extinction properties for each lognormal mode online as a function of aerosol composition and size, which are then utilised directly within the UM's radiative transfer code (Bellouin *et al.*, 2013). Each aerosol species requires prescribed spectral refractive indices (RI) spanning the electromagnetic spectrum from ultra-violet (0.2 µm) to radiowave (1 cm) wavelengths. Ammonium nitrate RIs have previously been compiled for an older generation of the UM

335 (HadGEM2-ES) (Bellouin *et al.*, 2011). For $NH_4 \cdot NO_3$, real and imaginary RIs for the wavelength spectrum 2-20 µm are taken from Jarzembski *et al.* (2003), while RIs for > 20 µm are assumed to be that at 20 µm. Real RIs for 0.59-1.61 µm are from CRC Handbook of Chemistry and Physics (Weast, 1971) and are then extended to cover the 0.1-2 µm spectrum. Imaginary RIs for the ultraviolet and visible spectra (< 0.7 µm) are arbitrarily set to a small number assuming little absorption (1×10^{-8}).

340 To optically represent the coarse NO_3 aggregate hetNO_3, $NaNO_3$ spectral RIs have been compiled from the literature for this study. RI values are mostly from the tabulated data of Palik and Khanna (1998) and references therein for solid birefringent $NaNO_3$ crystals. From 0.23-0.42 µm, imaginary RIs are determined by applying the Beer-Lambert law to Cleaver *et al.* (1963)

Atmospheric
Chemistry
and Physics
Discussions

Open Access

EGU

absorption coefficients and assuming a lattice thickness of 3 μm, as in Jacobson (1999). This approach is necessary to account for the second UV absorption peak missing in the data of Palik and Khanna (1998). Imaginary RIs for wavelength spectrum

345 0.42-5.88 μm appear not to have been measured and are pragmatically set to the observed values for $NH_4 \cdot NO_3$, which are from Gosse *et al.* (1997) for 0.7-2 μm and from Jarzembski *et al.* (2003) for 2-5.88 μm. As is the case for $NH_4 \cdot NO_3$, imaginary RIs are set to an arbitrary small number (1×10^{-8}) from 0.42-0.7 μm to reflect the little or no absorption in that spectrum (Palik and Khanna, 1998). For the real RIs, in the 0.4-0.65 μm spectrum values are from Cotterell *et al.* (2017) for measurements at 0 % relative humidity. From 0.66-0.67 μm, the real RIs are provided by Ballard *et al.* (1972) and for 0.7 μm from Ivlev and Popova

350 (1974). Above wavelengths of 1 mm - the scope of the Palik and Khanna (1998) database - the real and imaginary RIs are set to the value at 1 mm. The compiled spectral RIs for $NH_4 \cdot NO_3$ and $NaNO_3$ are shown in Fig. S5 in the Supplement and tabulated in Tables S3 and S4 in the Supplement.

The default configuration of UKCA-mode and by extension UKCA-Radaer, as used in UKESM1 and HadGEM3-GC3.1,

355 represents tropospheric SO_4 with $(NH_4)_2 \cdot SO_4$ refractive indices and (optionally) stratospheric SO_4 with sulphuric acid (H_2SO_4) refractive indices. This is internally inconsistent given that the tropospheric SO_4 is missing the considerable mass associated with NH_4. The new UKCA-mode nitrate configuration presented here that includes SO_4, NO_3, and NH_4 as separate tracers firstly apportions NH_4 mass to NO_3 using a 1:1 molar ratio and the NH_4 remainder to SO_4 using a 2:1 molar ratio (represented by $NH_4 \cdot NO_3$ and $(NH_4)_2 \cdot SO_4$ refractive indices respectively), and then represents remaining SO_4 mass with H_2SO_4 refractive

360 indices. Another internal inconsistency in the default UKCA-mode configuration is that NH_4 is not explicitly represented during hygroscopic growth (i.e. in the ZSR algorithm), owing to the lack of an NH_4 tracer. In the new nitrate scheme, NH_4, NO_3, and $hetNO_3$ are explicitly added to the hygroscopic growth routine, with NH_4 counteracting hygroscopic aerosol growth and NO_3 and $hetNO_3$ promoting it.

2.3 Simulation design

365 The scientific purpose of this study is to investigate whether representing the kinetic limitation of HNO_3 condensation onto pre-existing aerosols during the production of ammonium nitrate significantly alters the resulting atmospheric concentrations of ammonium nitrate and, indirectly, coarse nitrate aerosol. To this end, four sensitivity simulations are performed with the UM and the new nitrate scheme: 1. A control simulation with no nitrate aerosol and the default UKCA-mode setup 2 (i.e. standard GA7.1) (CNTL); 2. A simulation with $NH_4 \cdot NO_3$ reaching equilibrium instantaneously (INSTANT); 3. A simulation

370 with the HNO_3 uptake rate set to $\gamma = 0.193$ in Eq. 7 following Feng and Penner (2007) (FAST); and 4. A simulation with the HNO_3 uptake rate set to $\gamma = 0.001$ in Eq. 7 following Bauer *et al.* (2007) (SLOW). These simulations are further listed in Table 2 and were selected to span the range of HNO_3 uptake rates on standard atmospheric particles from the literature (Bauer *et al.*, 2007). All simulations are run for 25 model years with only the last 20 years used for analysis.

375

Simulation name	Description
CNTL	Control simulation - no nitrate aerosols
INSTANT	Nitrate aerosols – instantaneous equilibrium for NH_4NO_3 ($\tau = 0$ in Eq. 8)
FAST	Nitrate aerosols– fast uptake coefficient for NH_4NO_3 ($\gamma = 0.193$ in Eq. 7)
SLOW	Nitrate aerosols– slow uptake coefficient for NH_4NO_3 ($\gamma = 0.001$ in Eq. 7)

Table 2: A description of the UM simulations performed in this study

380   In these simulations, GA7.1 is forced by fixed sea surface temperature and sea ice fields prescribed as monthly climatologies for the year 2000, created by averaging over 1995-2004 the time-series data generated for CMIP6 atmosphere-only simulations. Additionally, aerosol and gaseous emissions are primarily prescribed as monthly fields from the CMIP6 historical emissions inventory (DECK/ Historical CMIP6 version 6.2.0), averaged over the 1995-2004 time-period. Table S2 in the Supplement gives global and annual total emissions for each of the UKCA chemical species. The CMIP6 emissions inventory was derived

385   from the Community Emissions Data System (CEDS) project which is documented by van Marle *et al.* (2017), Hoesly *et al.* (2018) and Feng *et al.* (2020); while its integration within the UM is detailed by Sellar *et al.* (2020). The simulation design (i.e. perpetual year 2000 conditions) follows standard simulation protocol for UKCA model development in the Met Office.

Global anthropogenic NH_3 emissions in the year 2000 from CEDS amount to 50 Tg yr^{-1}, in vast excess of equivalent emissions

390   from the CMIP5-derived MACCitty inventory of 37.5 Tg yr^{-1} (Granier *et al.*, 2011). Hoesly *et al.* (2018) attribute this disparity to differing assumptions in agricultural NH_3 trends and to the lack of consideration for wastewater and human waste NH_3 emissions in MACCity. Oceanic NH_3 emissions in these simulations – which account for 26 % of total NH_3 emissions – follow Bouwman *et al.* (1997) and biomass-burning emissions are described by van Marle *et al.* (2017). NH_3 exhibits a strong seasonal cycle with global emissions in June-August ~50 % greater than in December-February (Fig. S6b in the Supplement). The

395   global NH_3 source of ~65 Tg yr^{-1} in these simulations is close to the model-mean value of 63 Tg yr^{-1} for GCMs participating in the AeroCom phase III nitrate experiment (Bian *et al.*, 2017). Nitrogen oxide (NO_x) emissions from anthropogenic, biomass-burning and aircraft sources are prescribed as monthly fields from the CEDS inventory (van Marle *et al.*, 2017; Hoesly *et al.*, 2018). NO_x emissions from soils are taken from Yienger and Levy (1995), corrected to a total source of 12 Tg[NO] yr^{-1} (Sellar *et al.*, 2020). The global and annual total NO_x emissions amount to 106 Tg[NO] yr^{-1}. Further details on gas and aerosol

400   emissions in these simulations is provided in Section S3 in the Supplement.

3 Results

3.1 Global and annual mean metrics

Table 3 shows global tropospheric and annual mean budgets for HNO_3, NH_3, NO_3, and NH_4 from the FAST and SLOW
simulations alongside equivalent metrics from the present day simulations of Xu and Penner (2012) (hereafter XP12),
405 Hauglustaine *et al*. (2014) (hereafter HA14), and from the AeroCom model intercomparison project detailed by Bian *et al*.
(2017) (hereafter BI17). The INSTANT simulation is near-indistinguishable from FAST using these metrics (Table S5 in the
Supplement) - suggesting that $NH_4.NO_3$ concentrations in FAST reach thermodynamic equilibrium near instantaneously - and
INSTANT is thus omitted from further analysis. With respect to Table 3 and to the rest of the Results section, 'fine NO_3' refers
to NO_3 associated with NH_4 while 'coarse NO_3' refers to NO_3 associated with dust and sea-salt (i.e. NO_3 in $hetNO_3$).

410

The net HNO_3 production rates in FAST (44.1 Tg[N] yr^{-1}) and SLOW (44.2 Tg[N] yr^{-1}) are comparable to equivalent rates in
HA14 (45.1 Tg[N] yr^{-1}) and XP12 (38 Tg[N] yr^{-1}). Additionally, the NH_3 emissions in FAST and SLOW (53.5 Tg[N] yr^{-1}) are
comparable to HA14, XP12, and BI14 (50.5, 53.6, and 51.8 Tg[N] yr^{-1} respectively) suggesting that to the first order the
ammonium and nitrate precursor gas emissions are commensurate on a global basis with prior studies. Total NO_3 (i.e. fine +
415 coarse) production in the FAST (22.9 Tg[N] yr^{-1}) and SLOW (19.9 Tg[N] yr^{-1}) simulations is significantly greater than in
HA14 (14.4 Tg[N] yr^{-1}) and XP12 (16 Tg[N] yr^{-1}) and at the upper range of the AeroCom models in BI17 (Mean = 13.7, Range
= 1.5 to 28.2 Tg[N] yr^{-1}). This is also the case for NH_4 production rates where FAST (30.4 Tg[N] yr^{-1}) and SLOW (25.6 Tg[N]
yr^{-1}) exceed equivalent values in HA14 (17.5 Tg[N] yr^{-1}) and BI17 (Mean = 23.7, Range = 17.8 to 29.5 Tg[N] yr^{-1}), and are
comparable with XP12 (30.5 Tg[N] yr^{-1}). This suggests that NH_4 and NO_3 aerosol production in the UM is at the upper end of
420 efficiency when compared to other existing climate models.

Significant differences between the FAST and SLOW simulations are highlighted by the global NO_3 metrics in Table 3. In
particular, the fine NO_3 source is 6.3 Tg[N] yr^{-1} in FAST but only 2.7 Tg[N] yr^{-1} in SLOW, marking a 57 % decrease.
Conversely, SLOW exhibits 5 % more coarse NO_3 production than in FAST. The difference is equally discernible in the
425 burdens, with 47 % of the total NO_3 burden as coarse NO_3 in FAST compared to 67 % in SLOW. This can be compared to a
72 % coarse fraction in HA14 and 47 % in XP12. The total NO_3 burdens of 0.2 Tg[N] in FAST and 0.15 Tg[N] in SLOW are
commensurate with 0.18 Tg[N] in HA14, 0.17 Tg[N] in XP12, and the AeroCom median of 0.14 Tg[N] in BI17. The NH_3
burden in FAST (0.04 Tg[N]) is at the lower end of the AeroCom range in BI17 (0.04 to 0.7 Tg[N]) while the NH_4 burden in
FAST (0.42 Tg[N]) is at the upper range of BI17 models (0.13 to 0.58 Tg[N]) which corroborates the assertion that NH_4 and
430 NO_3 aerosol production in the UM is at the upper end of efficiency when compared to other existing climate models, and
suggests that NH_3 rather than HNO_3 is the limiting factor controlling $NH_4.NO_3$ production in these simulations. In summary,
Table 3 illustrates the close parity with regards global and annual mean metrics between the UM simulations and previous
nitrate simulations with various climate models from the literature.

				FAST	SLOW	XP12	HA14	BI17
HNO$_3$	Source	Gas phase	Tg[N] yr^{-1}	35.2	35.7	24.4	44.6	[82, 92]
		Aerosol phase		18.6	18.2	17.9	3.9	[4.7, 28.5]
		Total		53.8	53.9	42.3	48.5	-
	Loss	Gas phase	Tg[N] yr^{-1}	9.7	9.7	4.3	3.4	[47, 66]
		Fine nitrate		6.4	2.7	8.8	3.2	[2, 9.5]
		Coarse nitrate		16.6	17.3	7.2	11.2	-
		Dry deposition		6	8	7.8	14.7	10.9 [8, 16.4]
		Wet deposition		14.9	15.8	14.5	17	25.1 [11, 37.2]
		Total		53.4	53.4	42.6	49.5	-
		Wet fraction	%	71.4	66.4	65	53.6	68.6 [57.8, 76.3]
	Burden		Tg[N]	0.48	0.48	0.3	0.3	0.56 [0.15, 1.27]
	Lifetime		days	3.2	3.2	4.8	2.3	[3.5, 5.7]
NO$_3$	Source	Fine nitrate	Tg[N] yr^{-1}	6.3	2.7	8.8	3.2	-
		Coarse nitrate		16.6	17.3	7.2	11.2	-
		Total		22.9	19.9	16	14.4	13.7 [1.5, 28.2]
	Loss	Dry deposition	Tg[N] yr^{-1}	8.9	8.3	4	1.7	4.7 [0.3, 10.8]
		Wet deposition		14.3	11.8	12	12.7	9.9 [1.2, 20.5]
		Total		23.2	20.1	16	14.4	13.7 [1.5, 28.3]
		Wet fraction	%	61.7	58.6	75	88.2	77 [56.3, 90.8]
	Burden	Fine nitrate	Tg[N]	0.11	0.05	0.09	0.05	-
		Coarse nitrate		0.09	0.1	0.08	0.13	-
		Total		0.2	0.15	0.17	0.18	0.14 [0.03, 0.42]
	Lifetime	Fine nitrate	days	6.2	7.2	3.7	5.6	-
		Coarse nitrate		2	2	4	4.2	-
		Total		3.2	2.7	3.9	4.6	5 [2, 7.8]
NH$_3$	Source	Emissions	Tg[N] yr^{-1}	53.5	53.5	53.6	50.5	51.8 [46.9, 58.1]
	Loss	Gas phase	Tg[N] yr^{-1}	-	-	-	0.6	-
		NH$_4$ formation		30.4	25.6	30.5	17.5	26.4 [18.4, 34.6]
		Dry deposition		17.4	20.4	12.7	21.3	15.4 [10.4, 24.1]
		Wet deposition		5.7	7.5	9.6	11.1	11 [5.6, 15.3]

Atmospheric
Chemistry
and Physics
Discussions
Open Access
EGU

		Total		53.4	53.5	53.6	50.5	53.2 [49.8, 57.9]
		Wet fraction	%	24.6	27	43	34.3	40.7 [24.5, 58.1]
	Burden		Tg[N]	0.04	0.06	0.07	0.09	0.16 [0.04, 0.7]
	Lifetime		days	0.28	0.41	0.46	0.63	0.72 [0.29, 0.98]
NH_4	Source	NH_3 conversion	Tg[N] yr^{-1}	30.4	25.6	30.5	17.5	23.7 [17.8, 29.5]
	Loss	Dry deposition	Tg[N] yr^{-1}	5.7	4.7	4.5	2.5	4.5 [1.3, 16.3]
		Wet deposition		24.9	21	25.9	14.9	20.7 [5.6, 34.6]
		Total		30.5	25.7	30.4	17.4	25.2 [17.7, 37.4]
		Wet fraction	%	81.4	81.8	85.2	85.6	81 [25.6, 94.7]
	Burden		Tg[N]	0.42	0.36	0.26	0.22	0.25 [0.13, 0.58]
	Lifetime		days	5	5	3.2	4.5	4.3 [1.9, 9.8]

Table 3: Global and annual-mean metrics for nitric acid (HNO₃), nitrate (NO₃), ammonia (NH₃) and ammonium (NH₄) in the FAST and SLOW simulations compared to Xu and Penner (2012), Hauglustaine *et al*. (2014) (HA14) and the AeroCom phase III model intercomparison project described in Bian *et al*. (2017) (BI17). Square brackets in the BI17 column denoted the AeroCom inter-model range.

3.2 Annual mean burdens and concentrations

Figure 1 shows the annual-mean mass burdens of NH_4, NO_3 and $hetNO_3$ in the FAST and SLOW simulations. While units of mg[N]m^{-2} are used in Fig. 1, units of 'mg of substance per m^2' are used in the following text for direct comparison with HA14. Fine NO_3 associated with NH_4 is concentrated over land regions, particularly in the Northern Hemisphere. The fine NO_3 burden averaged over European land is 1 mg[NO_3]m^{-2} in SLOW and 3 mg[NO_3]m^{-2} in FAST. The total NO_3 over Europe is 3 mg[NO_3]m^{-2} in SLOW and 5 mg[NO_3]m^{-3} in FAST, which is close to the simulated present day values of 3-4 mg[NO_3]m^{-2} in HA14. Fine NO_3 peaks in Europe over the Mediterranean at 5 mg[NO_3]m^{-2} in SLOW and 12 mg[NO_3]m^{-2} in FAST. South Asia exhibits the greatest regional fine NO_3 burdens with 8 mg[NO_3]m^{-2} in SLOW and 14 mg[NO_3]m^{-2} in FAST. The total NO_3 burdens over South Asia of 11 mg[NO_3]m^{-2} in SLOW and 15 mg[NO_3]m^{-2} in FAST are somewhat greater than equivalent values in HA14 of 5-10 mg[NO_3]m^{-2}. Conversely, the total NO_3 concentrations in East Asia (China) are smaller in these simulations (5 mg[NO_3]m^{-2} in SLOW and 9 mg[NO_3]m^{-2} in FAST) than in HA14 (10-20 mg[NO_3]m^{-2}). Over Central North America, the total NO_3 burden is 2 mg[NO_3]m^{-2} in SLOW and 5 mg[NO_3]m^{-2} in FAST, which compares to 3-4 mg[NO_3]m^{-2} in HA14. Reconciling all these inferences, FAST exhibits twice as much fine NO_3 burden on average as does SLOW. Whereas fine NO_3 burdens are concentrated over land, coarse NO_3 (i.e. $hetNO_3$) is more evenly spread over the Earth and prevalent over maritime areas where it forms on sea-salt and aged dust particles (Figs 1g,h). Over European land, coarse NO_3 constitutes 31 % of the total NO_3 burden in FAST and 63 % in SLOW. Equivalent figures for East Asia are 15 and 30 %; South Asia – 10
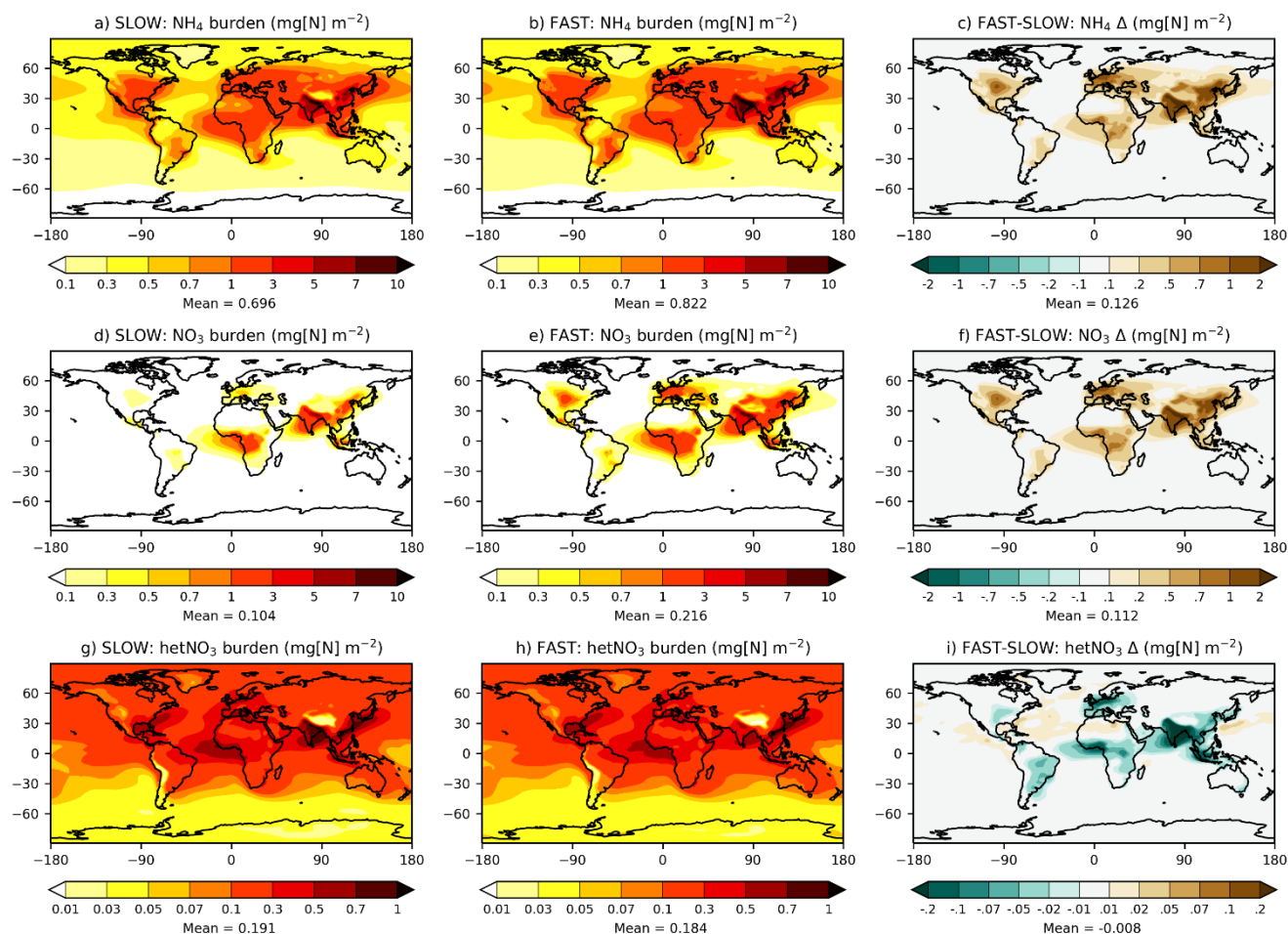
Atmospheric
Chemistry
and Physics
Discussions
Open Access

Figure 1: Annual-mean NH₄, NO₃, and hetNO₃ burdens from the SLOW and FAST simulations

and 23 %; and Eastern North America – 45 and 83 %. Therefore, the partitioning of NO₃ between the coarse and fine modes is highly sensitive to the uptake rate of HNO₃ on ambient aerosol.

Figure 2 shows maps of annual-mean near-surface concentrations of NH₄, NO₃ and hetNO₃ in the SLOW and FAST simulations. The spatial distributions of fine NO₃ are similar to those reported in BI17 and HA14 with peak concentrations over North America, Europe, South Asia, South East Asia, and East Asia land regions, coincident with the highest NH₃ and NOₓ emitting regions (Figure S6 in the Supplement). The average total NO₃ concentrations over Europe are 1.5 and 3.5 $\mu g[NO_3]m^{-3}$ in SLOW and FAST respectively, which can be compared to 4-5 $\mu g[NO_3]m^{-3}$ in HA14. In Central North America, total NO₃ concentrations amount to 1 and 3 $\mu g[NO_3]m^{-3}$ on average in SLOW and FAST, with 50 % and 15 % contributions from coarse NO₃. The regional-mean total NO₃ concentrations in East Asia amount to 3.5 and 6.5 $\mu g[NO_3]m^{-3}$ and in South

Atmospheric
Chemistry
and Physics
Discussions
Open Access
EGU
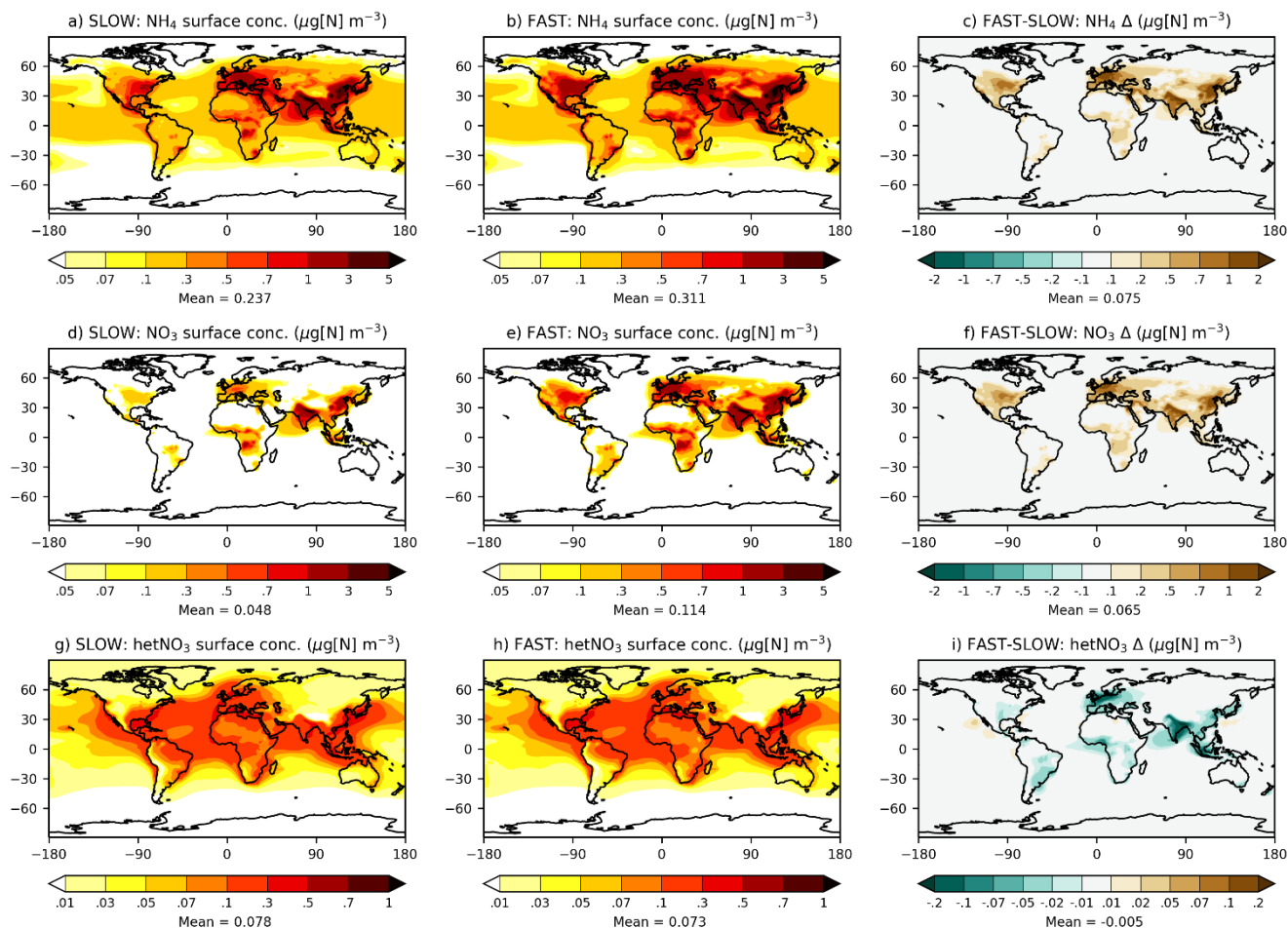
Figure 2: Annual-mean NH₄, NO₃, and hetNO₃ near-surface concentrations from the SLOW and FAST simulations

Asia amount to 5.5 and 7.5 µg[NO₃]m⁻³, in SLOW and FAST respectively. Total NO₃ differences between FAST and SLOW are driven by changes to the fine NO₃ concentrations (Figs 2d-f), with comparatively minimal changes to coarse NO₃ (Figs 2g-i).

Figure 3 shows the zonal mean, vertical distribution of NO₃, NH₄ and hetNO₃ aerosol in the FAST and SLOW simulations. NH₄ reaches a greater altitude than fine NO₃ owing to its long-lived association with SO₄ aerosol (Figs 3a-b). Due to the high solubility of NH₃ gas and thus swift wet removal from the atmosphere, free ammonia is mostly limited to the bottom 1 km of the atmosphere (Bellouin *et al.*, 2011), which limits the vertical extent to which NH₄·NO₃ may form (Figs 3c-d). This is further corroborated by Figure S8 in the Supplement which shows the 'gas ratio', defined as $([NH_3] + [NH_4] - 2 \times [SO_4])$ divided
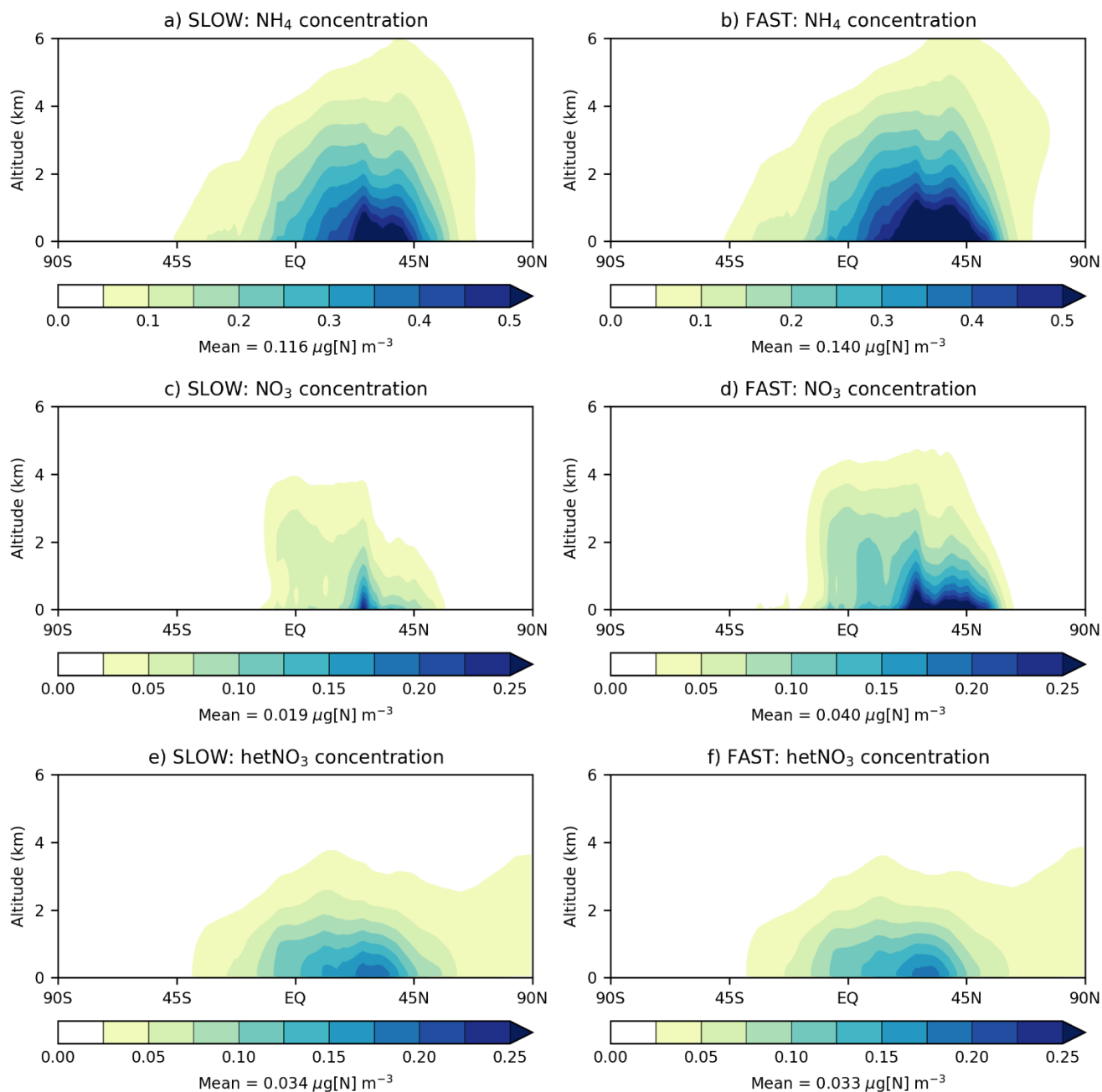
Figure 3: Annual and zonal-mean NH₄, NO₃, and hetNO₃ concentrations vs altitude from the SLOW and FAST simulations

485   by $([HNO_3] + [NO_3])$, with values greater than 1 indicating that conditions are HNO_3-limited and less than 1 indicating conditions are NH_3-limited (Ansari and Pandis, 1998). It is clear from Fig. S8 that $NH_4 \cdot NO_3$ production is HNO_3- limited at
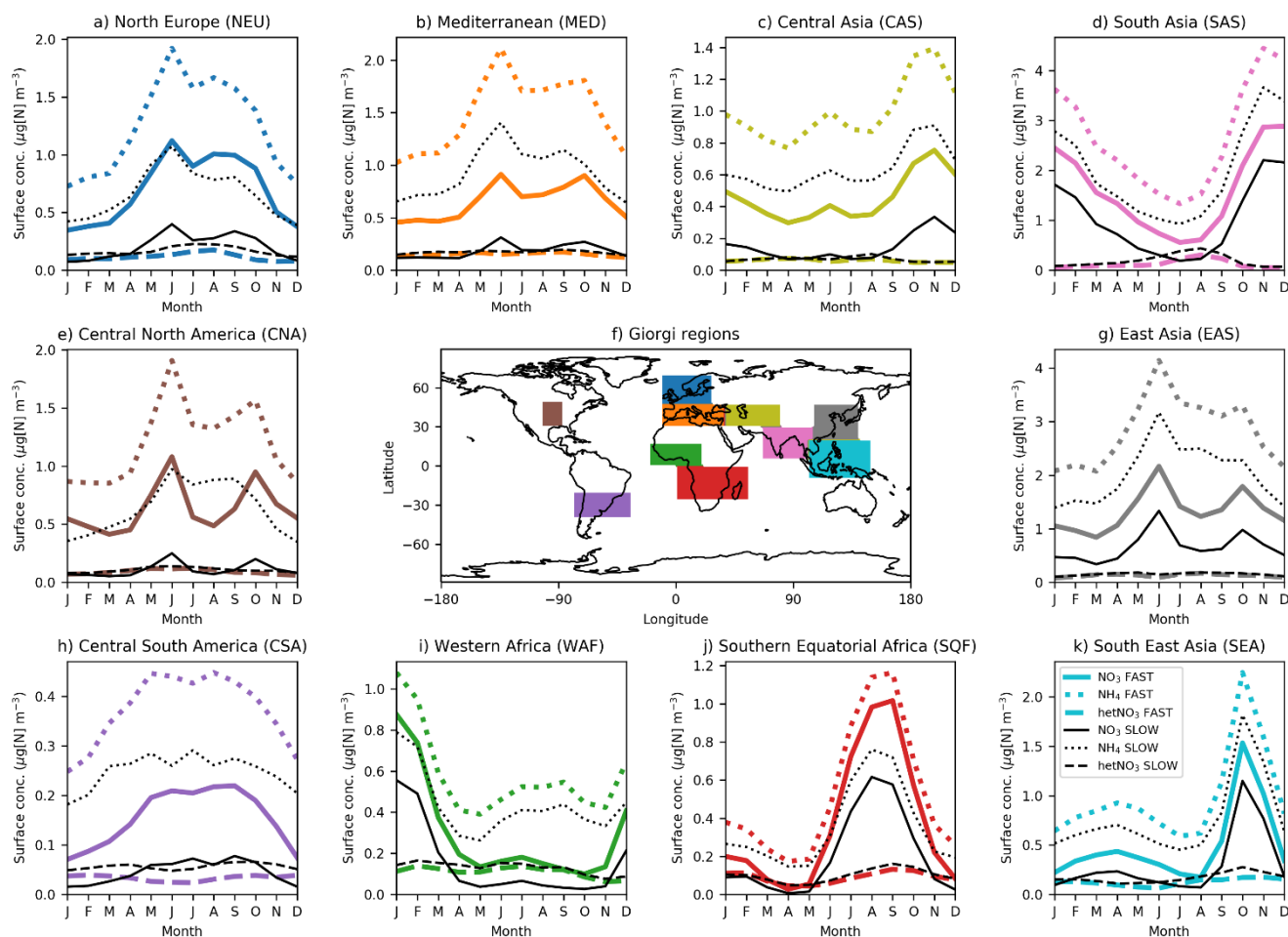
Figure 4: Regional and monthly-mean NH₄, NO₃, and hetNO₃ near-surface concentration time-series for the SLOW and FAST simulations for 10 'Giorgi regions' [Giorgi, 2006] (land-only) representing high NO₃ concentration areas.

490

the surface over land regions but that conditions are ubiquitously NH_3-limited above altitudes of 1000 m. While $NaNO_3$ and $Ca(NO_3)_2$ are not volatile like $NH_4 \cdot NO_3$, they are instead associated with coarse particles that are readily removed from the atmosphere by gravitational sedimentation and wet scavenging, and thus remain confined to the lowest 1 km of the atmosphere (Figs 3e-f).

495 **3.3 Regional surface concentrations**

Figure 4 shows the seasonal trends in NO_3, NH_4 and $hetNO_3$ near-surface concentrations averaged over land in 10 'Giorgi' regions (Giorgi, 2006), selected due to their high fine NO_3 concentrations (Fig. 2). For most of the regions (NEU, MED, CNA, EAS, WAF, SQF, and SEA), NH_4 and fine NO_3 trends in both the FAST and SLOW simulations are tightly coupled to trends

500 in regional NH_3 emissions (Figure S7 in the Supplement), which further corroborates the notion that $NH_4\cdot NO_3$ formation may be limited in these regions by available NH_3. $NH_4\cdot NO_3$ concentrations in the CAS, SAS, and CSA regions may be more dependent on seasonal meteorology than other regions, for instance SAS (i.e. South Asia) experiences a strong summer monsoon which would enhance wet deposition of $NH_4\cdot NO_3$ during summer and thus reduce concentrations. SAS also has consistently elevated NH_3 concentrations throughout the year and is thus less sensitive to seasonal trends in NH_3 emissions

505 (Zhu *et al.*, 2015). In all regions, NH_4 and fine NO_3 concentrations exhibit a strong seasonal cycle in both SLOW and FAST while the seasonal cycle in coarse NO_3 is less apparent. In the SLOW simulation, coarse NO_3 concentrations are of similar magnitude to fine NO_3 concentrations in NEU, MED, CAS, CAN, CSA, and WAF on a regional-mean basis (Fig. 4).

Figures 5 and 6 show the near-surface concentrations of HNO_3, NH_4 and total NO_3 over the US (Fig. 5) and Europe (Fig. 6) in the FAST and SLOW simulations compared to observations from the Clean Air Status and Trends Network (CASTNet,

510 www.epa.gov/castnet, last access: January 2021, Finkelstein *et al.* (2000)) for the US and the European Monitoring and Evaluation Programme (EMEP, http://ebas.nilu.no/, last access: March 2021, Torseth *et al.* (2012)) for Europe. In both networks the sites are located so as to represent the wider region. Data processing and site selection for the observations follows the methodology described in Hardacre *et al.* (2021), who have compared SO_2 and SO_4 concentrations from UKESM simulations with CASTNet and EMEP observations. CASTNet and EMEP data are averaged over the period 1994-2013 where

515 available. For CASTNet there are a total of 16 Western sites and 33 Eastern sites (49 in total) that meet data processing criteria in this study (where the east-west delineation is described in Hardacre *et al.* (2021)). For EMEP there are 59 sites for HNO_3, 59 sites for NH_4 and 80 sites for NO_3 meeting data processing criteria over the 1994-2013 timeframe. For the scatterplots in Figs 5 and 6, model output is linearly interpolated to measurement sites. It is important to note that the absolute magnitudes of concentrations are not directly comparable between the simulations and observations given that the simulations assume

520 constant NO_x and NH_3 emissions based on the year 2000 whereas NO_x and NH_3 emissions in reality are transient. This becomes apparent when comparing the network-mean concentrations in the simulations with the observations (Figure S9 in the Supplement) where there is a clear negative trend in HNO_3, NH_4 and NO_3 concentrations in both CASTNet and EMEP observations from 1994 to 2013.

525 Figure 5 shows that the spatial distributions of HNO_3, NO_3 and NH_4 over the US are similar in FAST and SLOW, with peak HNO_3 concentrations in the east and midwestern states reflecting industrial NO_x emissions, and peak NO_3 and NH_4 in the midwestern and central states reflecting agricultural NH_3 emissions (Park *et al.*, 2004). The absolute magnitudes of NH_4 and NO_3 concentrations are closer to CASTNet observations in SLOW (Fig. 5j) than in FAST (Fig. 5k), but the spatial correlation coefficients are better in the eastern US in FAST ($R = 0.87$ for NH_4 and $R = 0.61$ for NO_3) than in SLOW ($R = 0.77$ for NH_4

530 and $R = 0.06$ for NO_3). This suggests that the positive NO_3 (and correspondingly NH_4) biases in FAST may emanate from a surplus of HNO_3 in the model, given that HNO_3 is positively biased in the eastern US in both FAST and, to an even greater extent, SLOW (Fig. 5d).

Atmospheric
Chemistry
and Physics
Discussions
Open Access
EGU
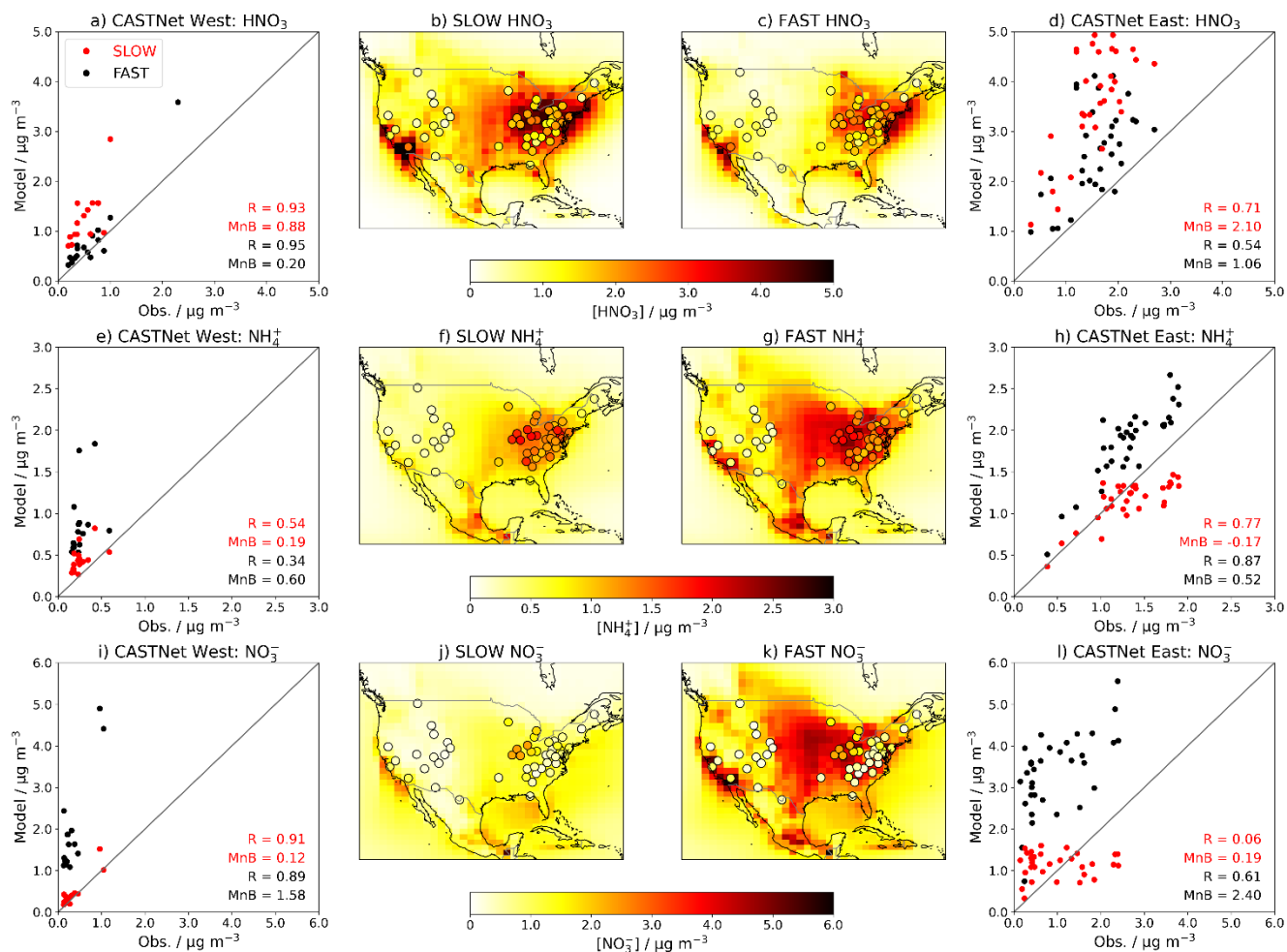
Figure 5: Annual-mean HNO₃, NH₄ and total-NO₃ near-surface concentrations in the FAST and SLOW simulations over North America compared to CASTNet observations averaged over 1994-2013. In (b), (c), (f), (g), (j) and (k), coloured contours show simulated concentrations while overlayed filled circles represent CASTNet observations. In (a), (d), (e), (h), (i) and (l), 'R' is the Pearson's correlation coefficient and 'MnB' is the mean bias between simulated and observed concentrations

Over Europe, NO_3 and NH_4 concentrations are closer to EMEP observations in the SLOW simulation than in the FAST simulation (e.g. smaller mean biases in Figs 6d,g). NO_3 concentrations in both FAST and SLOW peak in the Po Valley (North Italy) and Benelux Region (Belgium and the Netherlands), in anecdotal concordance with Druge *et al.* (2019) and references therein. The Po Valley peak in both the EMEP observations and simulations is due to the entrapment of industrial air pollution by regional geography. The observed NH_4 and HNO_3 peaks over the Czech Republic may be attributable to high agricultural NH_3 emissions pre-2004, with concomitant concentration declines owing to the Gothenburg protocol (Fortems-Cheiney *et al.*, 2016; Giannakis *et al.*, 2019). Neither of the observed NH_4 or HNO_3 concentration peaks in the Po Valley or the Czech
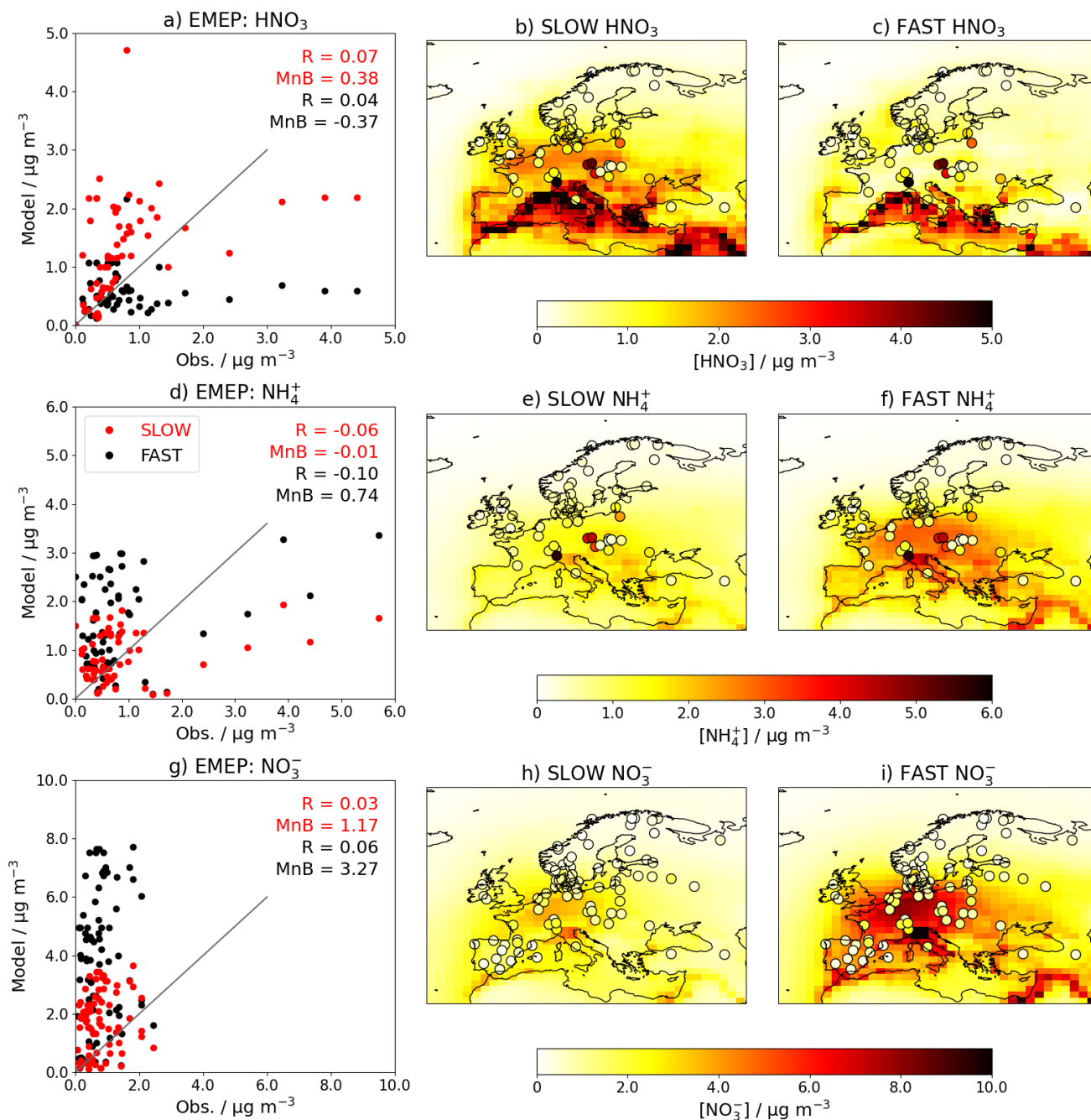
Figure 6: Annual-mean HNO₃, NH₄ and total-NO₃ near-surface concentrations for the FAST and SLOW simulations over Europe compared to EMEP observations averaged over 1994-2013 where available. In (b), (c), (e), (f), (h) and (i), coloured contours show simulated concentrations while overlayed filled circles represent EMEP observations. In (a), (d), and (g), 'R' is the Pearson's correlation coefficient and 'MnB' is the mean bias between simulated and observed concentrations

Republic are well captured by FAST or SLOW simulations which may be attributed to the coarse model resolution employed here (N96) and the close proximity of measurement sites to NH_3 sources.

555

Figure 7 shows the statistical distribution of 6 hourly total NO_3 and NH_4 concentrations from the FAST and SLOW simulations interpolated to two EMEP supersites in the UK – Auchencorth Moss and Chilbolton Observatory – and compared with observed diurnal concentrations from those sites (UK AIR, https://uk-air.defra.gov.uk/data/, last access: 29 January 2021). Both sites use MARGA instruments – a combination of wet rotating denuders for gas measurements, and stream jet aerosol

560 collectors for aerosol measurements – allowing for accurate partitioning between the aerosol and gas phases for volatile ammonium nitrate (Aas *et al.*, 2012; Twigg *et al.*, 2016). Only data recorded at the precise hours of 06:00, 12:00, 18:00, and 24:00 UTC that has passed the Department for Environment, Food & Rural Affairs' (DEFRA) quality control is utilised from the observations. Figure S10 in the Supplement shows the equivalent statistics for HNO_3 and NH_3 gases compared to observations. It is clear from Fig. 7 that NH_4 and NO_3 are significantly reduced in the SLOW simulation with respect to the

565 FAST simulation. It is also clear that the diurnal cycle, with NH_4 and NO_3 peaking at night (24Z or 00Z) and early morning (06Z) is both observed and skilfully simulated in both FAST and SLOW. Interestingly, the model shows similar biases to the Met Office's AQUM in: an over prediction of NO_3 during night-time in the summer; a slight under prediction of NO_3 in the winter; a large over prediction of HNO_3 during the day in the summer; and a smaller over-prediction of HNO_3 at night in the winter. The curious over-prediction of NH_3 at night in winter (Fig. S10 in the Supplement) was also observed in previous

570 incarnations of the AQUM and will be addressed in the UM in future by imposing a diurnal cycle to NH_3 emissions.

Figure 8 shows the seasonal cycle in total $PM_{2.5}$ concentrations in the CNTL, FAST, and SLOW simulations compared to collocated $PM_{2.5}$ observations from the Global Aerosol Synthesis and Science Project (GASSP; http://gassp.org.uk/data/, last access: 2 July 2020, Reddington *et al.*, 2017). GASSP amalgamates non-urban $PM_{2.5}$ measurements from three major networks:

575 The Interagency Monitoring of Protected Visual Environments (IMPROVE) project in North America, the European Monitoring and Evaluation Programme (EMEP), and Asia-Pacific Aerosol Database (A-PAD). The $PM_{2.5}$ analysis proceeds as in Turnock *et al.* (2020), with monthly-mean observations determined for each measurement site averaged over the years 2000-2010 and over each region. This is then compared with the simulated $PM_{2.5}$ output that has been linearly interpolated to individual site locations and averaged over the same time period and regions. Also shown in Fig. 8 is Modern-Era Retrospective

580 Analysis for Research and Applications, version 2 (MERRA-2) reanalysis data (Buchard *et al.*, 2017; Randles *et al.*, 2017), which closely follows GASSP surface observations in Europe and North America but is less successful in other regions where a smaller number of ground based observations are available, for example, incorrectly modelling the seasonal $PM_{2.5}$ cycles in South Asia and Pacific AUS NZ.
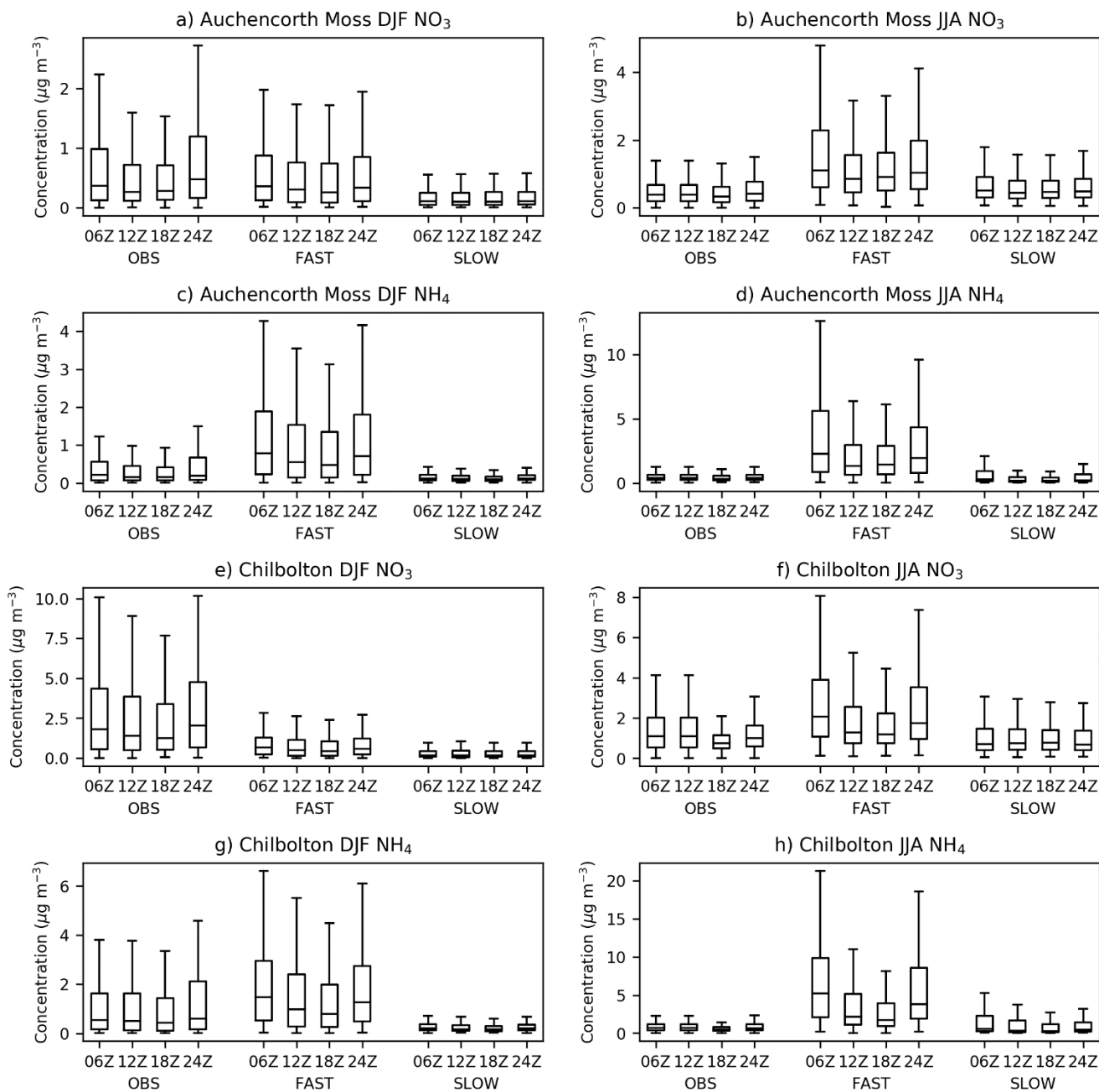
Figure 7: December-February (DJF) and June-August (JJA) diurnal cycles of near-surface total-NO₃ and NH₄ aerosol concentrations in the FAST and SLOW simulations interpolated to two European Monitoring and Evaluation Programme (EMEP) supersites in the UK – Auchencorth Moss [55.79216ºN, -3.2429ºE] and Chilbolton [51.149617ºN, -1.438228ºE], alongside 6 hourly observations from 2014-2015 for Auchencorth Moss and 2016-2020 for Chilbolton

585
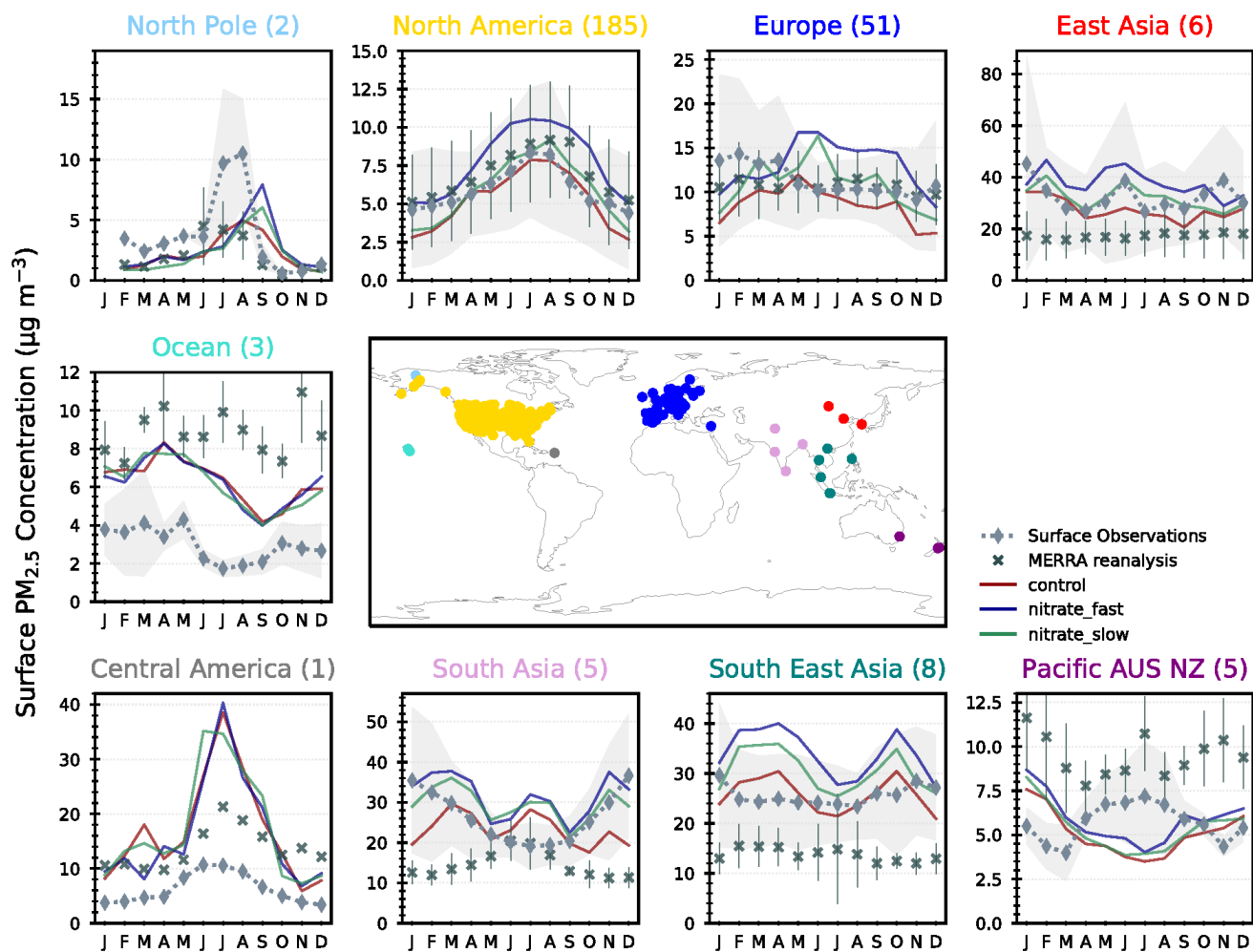
Figure 8: Regional and monthly-mean surface PM$_{2.5}$ concentrations in the UM simulations (red, blue green lines), CMIP6 ensemble means, and from MERRA reanalyses and GASSP surface observations

The largest observational networks in GASSP are over North America (IMPROVE) and Europe (EMEP). Over North America, the slight negative PM$_{2.5}$ bias in CNTL is brought closer to observations in SLOW and over-corrected in FAST which now exhibits a slight positive bias (Fig. 8). Over Europe observations suggest that PM$_{2.5}$ slightly peaks in DJF, which is not the case in any of the UM simulations in which PM$_{2.5}$ peaks in JJA. Druge *et al.* (2019) observed the same seasonal bias over Europe in the ALADIN-Climate regional model, which they attributed to uncertainties in the annual cycle of NH$_3$ and HNO$_3$ precursor gases. In Fig. 7, the simulated NH$_4$ concentrations in JJA vastly exceeded the observations at both UK-based supersites, indicating that summertime NH$_3$ gas emissions may be biased high in the prescribed CEDS emissions dataset over Europe. Over South Asia, East Asia, and South East Asia the CNTL simulation adeptly captures the seasonal PM$_{2.5}$ cycle and the addition of ammonium and nitrate in FAST and SLOW induces a slight positive bias. Figure 9 collates the annual mean
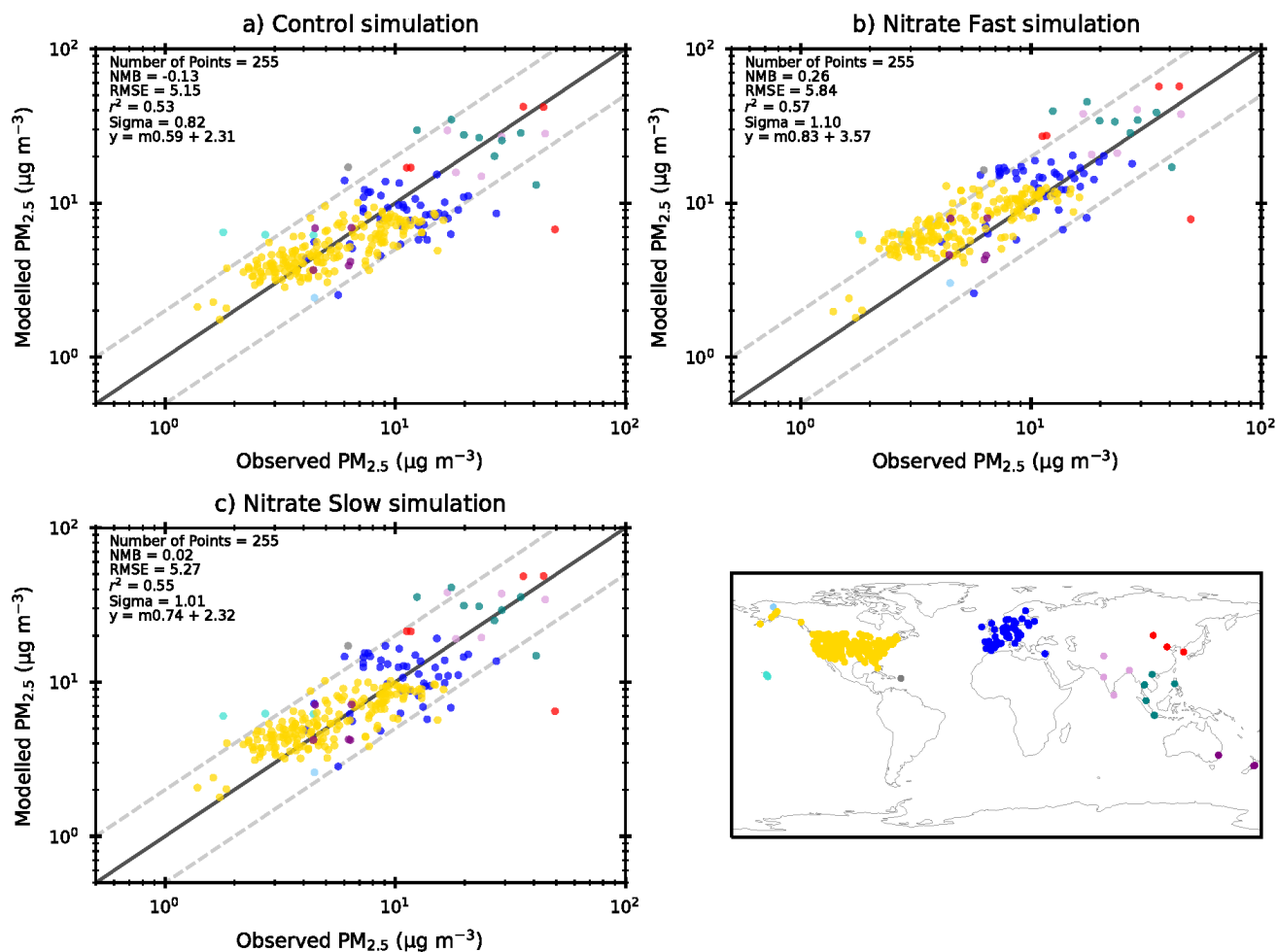
Figure 9: Scatterplots of observed vs simulated annual-mean PM2.5 concentrations in the CNTL, SLOW and FAST simulations accompanied with relevant statistics – the normalised mean bias (NMB), the root mean square error (RMSE), the correlation coefficient (r^2) and the ratio between standard deviations (Sigma)

observed and simulated $PM_{2.5}$ concentrations for each GASSP site, therefore statistics such as the normalised mean bias (NMB) are mostly weighted to the expansive North American and European networks. Nevertheless, it is interesting to note from Fig. 9 that the slight negative NMB in CNTL (-0.13) is completely compensated in SLOW (+0.02) and overcompensated in FAST (+0.26). However, all of the above inferences must be predicated on the fact the UM simulations use aerosol and gas emissions centred on the year 2000 whereas the observations are a composite of the years 2000-2010 and thus the temporal differences in emissions may partially explain disparities between the UM and observations. A robust result from Figs 8 and 9 is that both SLOW and FAST tend to increase $PM_{2.5}$ concentrations – particularly over Europe, Asia, and North America – with FAST inducing approximately double the $PM_{2.5}$ change than in SLOW.
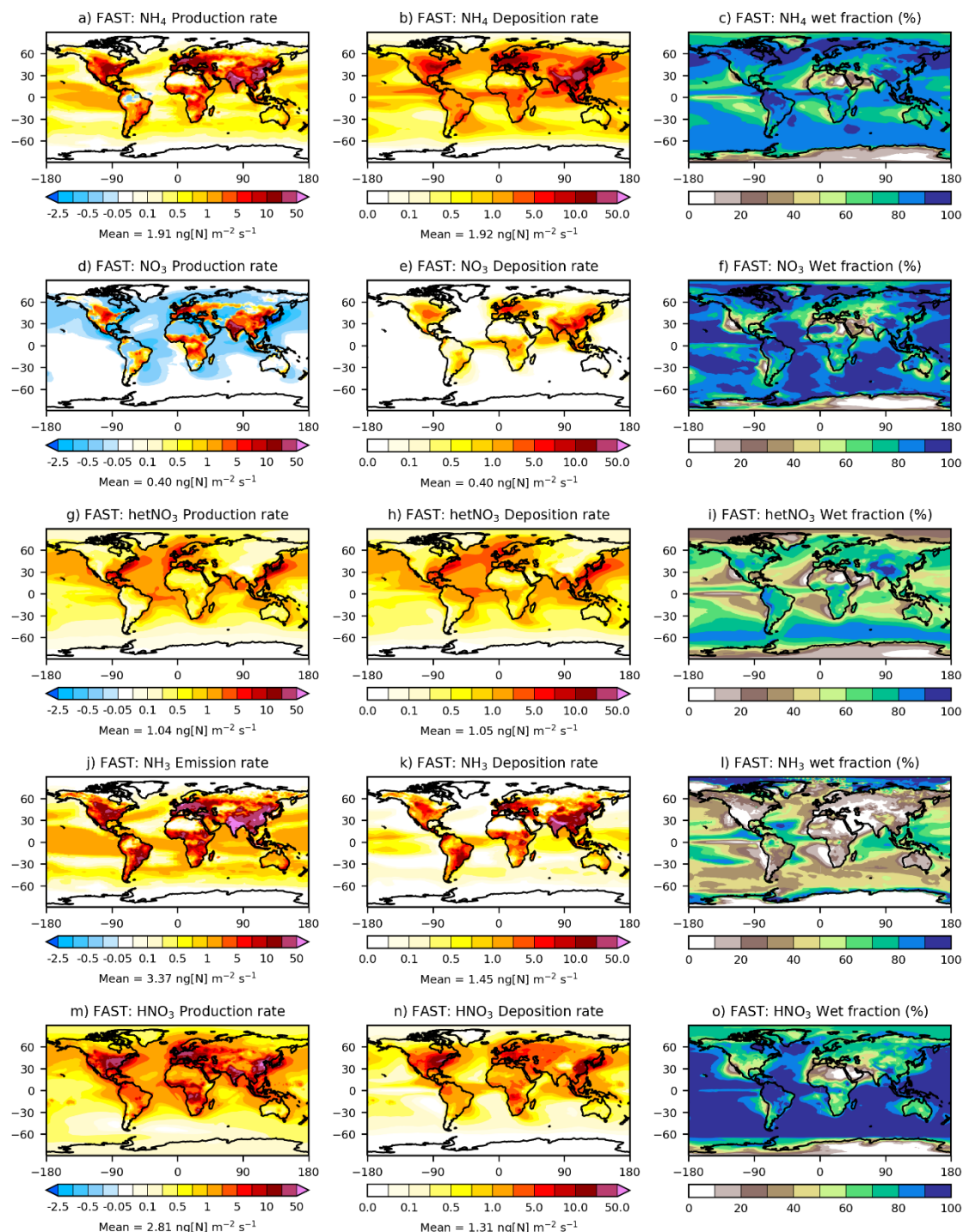
Figure 10: Annual-mean and column-integrated net-production and total deposition rates for NH₄, NO₃, hetNO₃, NH₃ and HNO₃, alongside the 'wet fraction' (the ratio of wet scavenging to total deposition), in the FAST simulation

3.4 Ammonium and nitrate production and deposition

620 Figure 10 shows the column-integrated annual-mean net production (or emission) rate, total deposition rate, and wet deposition fraction for NH_4, NO_3, $hetNO_3$, NH_3 and HNO_3 in the FAST simulation. NH_4 and fine NO_3 are primarily produced over land regions near NH_3 sources (Fig. 10j), with net NO_3 dissociation over adjacent land regions and oceans (Figs 10a,d). Figure S11 in the Supplement shows that whereas net NH_4 production is positive on a zonal-mean basis at altitudes up to 6 km, net fine NO_3 production is negative above 1 km north of 30°N latitude. Most fine NO_3 deposition is confined to land regions (Fig. 10e)

625 while coarse NO_3 is primarily deposited over oceans (Fig. 10h). Total deposition rates over land are 16, 5, and 4 Tg[N] yr^{-1} for NH_4, fine NO_3 and coarse NO_3 respectively and 18 and 12 Tg[N] yr^{-1} for NH_3 and HNO_3 gases respectively. Total deposition rates over oceans amount to 15, 2, and 13 Tg[N] yr^{-1} for NH_4, fine NO_3 and coarse NO_3 respectively and 15 and 9 Tg[N] yr^{-1} for NH_3 and HNO_3 gases respectively. This indicates that the dominant pathway for fixed nitrogen deposition to the oceans in these simulations, excluding river discharge sources, is via NH_4, NH_3 and coarse NO_3 deposition. The spatial distribution of

630 chemical production and deposition is similar in the FAST (Fig. 10) and SLOW (Fig. S12 in Supplement) simulations.

3.5 Aerosol optical depth and radiation changes

Figure 11 shows the annual-mean total aerosol optical depth at 550 nm (AOD_{550}) in the UM simulations (CNTL, FAST, and SLOW), with contributions from the Aitken, accumulation and coarse soluble modes, the Aitken insoluble mode, and mineral dust. Also plotted is the 2003-2012 mean MODIS 'collection 6' AOD_{550} satellite data, which merges NASA's "Dark Target"

635 and "Deep Blue" algorithms and is widely used for validating aerosol models (Levy *et al.*, 2013; Hsu *et al.*, 2013). It is clear that generally the CNTL simulation does a reasonable job of simulating the spatial distribution of AOD_{550} (Fig. 11a) when compared to MODIS (Fig. 11d).

The new nitrate scheme will impact the total AOD_{550} by various direct and indirect routes. Firstly, the addition of NO_3, NH_4

640 and $hetNO_3$ mass will increase the size and change the composition of the ambient aerosols thus altering their optical properties. Secondly, $hetNO_3$ mass associated with sea-salt will replace existing NaCl thus changing the aerosol composition. Thirdly, the explicit addition of NH_4 to the hygroscopic growth routine will reduce hygroscopic growth, whereas NO_3 and $hetNO_3$ will promote hygroscopic growth. Finally, tropospheric SO_4 was previously assumed to uniformly take the form of $(NH_4)_2SO_4$ in terms of optical properties, but in the new nitrate scheme is explicitly divided into H_2SO_4 and $(NH_4)_2SO_4$ contributions based

645 on NH_4 abundance. Indirectly, NH_4 and NO_3 may alter the AOD_{550} by impacting online aerosol emissions (such as dust and sea-salt) and atmospheric oxidant concentrations in the UM.

The AOD_{550} differences between the CNTL and nitrate simulations (FAST and SLOW) shown in Fig. 11 are a combination of the various direct and indirect changes to the UM listed above which do not necessarily result in an increase to AOD_{550}. The

650 global-mean AOD_{550} difference between FAST and CNTL of +0.0048 is serendipitously close to equivalent nitrate AODs in
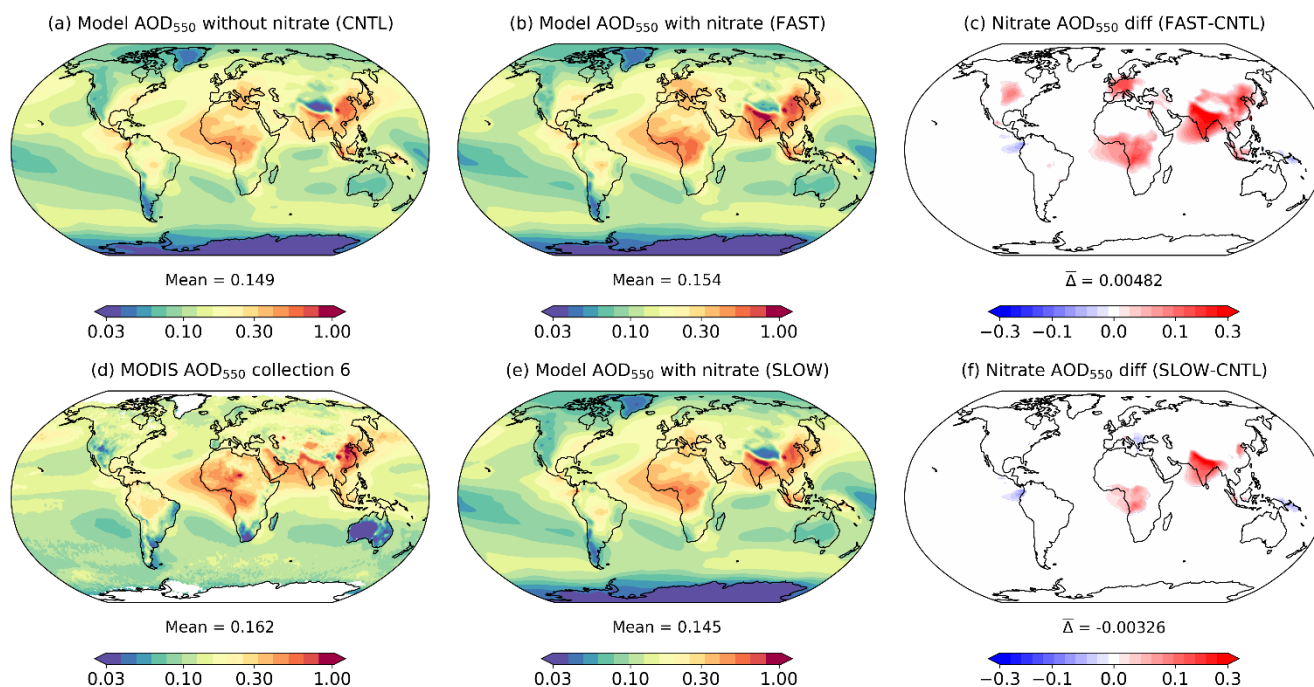
Figure 11: Annual-mean and column-integrated 550nm aerosol optical depth (AOD$_{550}$) in the CNTL, FAST, and SLOW simulations and from MODIS collection 6 satellite observations. (c) and (f) show the difference between the FAST and CNTL, and SLOW and CNTL, simulations respectively

655

the literature such as +0.006 in Paulot *et al*. (2016), +0.005 in HA14, and +0.006 [+0.002, +0.009] in Myhre *et al*. (2013), although it is important to note that the AOD$_{550}$ changes in those studies were derived from difference between present-day (PD) and pre-industrial (PI) simulations, rather than PD with and without nitrate. This is a subtle but important difference which reduces comparability given that the PI simulations included nitrate, albeit at much smaller concentrations than in PD

660   (Hauglustaine *et al.*, 2014). Despite the negligible global AOD$_{550}$ difference between FAST and CNTL, there are significant regional perturbations such as +0.05 over Northern Europe as a whole, +0.08 over East Asia, +0.19 over South Asia, and +0.04 over West Africa and Southern Equatorial Africa (Fig. 11c). The changes in the SLOW simulation are more subtle, for instance, AOD$_{550}$ changes by -0.007 over Northern Europe, +0.013 over East Asia, +0.1 over South Asia, and +0.018 over West Africa and Southern Equatorial Africa (Fig. 11f).

665

Figure 12 shows the annual-mean all-sky radiative flux perturbation at the Top-Of-the-Atmosphere (TOA). As the UM simulations are atmosphere-only with fixed sea-surface temperatures and sea-ice fields, the TOA radiative flux perturbation can also be denoted the total Effective Radiative Forcing (ERF) (Bellouin *et al*., 2020). The global-mean ERFs from FAST-CNTL and SLOW-CNTL are -0.19 Wm^{-2} and -0.07 Wm^{-2} respectively, which is a similar magnitude to the PD-PI nitrate RFs
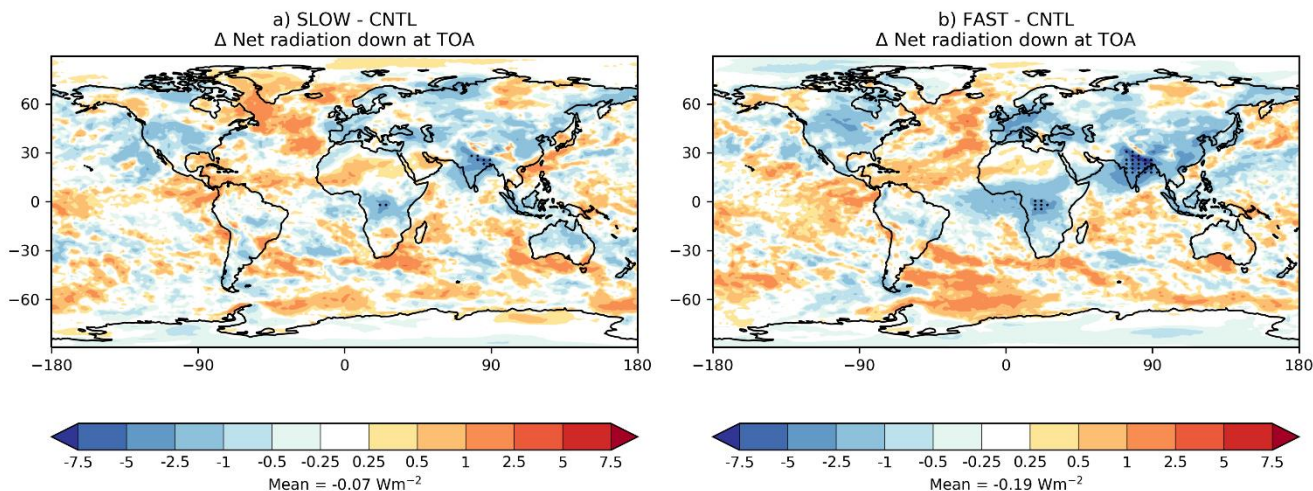
Figure 12: Annual-mean Top-Of-the-Atmosphere (TOA) net downwelling radiative flux (shortwave + longwave) perturbation or effective total radiative forcing in the a) SLOW and b) FAST simulations with respect to CNTL. Stippling indicates where differences are significant at the ±2σ level

of -0.056 Wm^{-2} in HA14, -0.17 Wm^{-2} in Bellouin *et al.* (2011), and -0.08 [-0.02, -0.12] Wm^{-2} in Myhre *et al.* (2013), although note again that the RFs in those studies were derived from difference between present-day (PD) and pre-industrial (PI) simulations, rather than PD with and without nitrate, and those studies determined the direct radiative forcing rather than the total ERF which also includes indirect radiative impacts of cloud and atmospheric composition changes. An explicit assessment of nitrate-induced changes to cloud properties is outside the scope of this study. Although most regions exhibit insignificant radiative differences between FAST and CNTL in Fig. 12b (where stippling indicates significant changes at the ±2σ level), there are significant changes over Europe (min = -3.7 Wm^{-2}, mean = -1.5 Wm^{-2}), South Asia (min = -10.3 Wm^{-2}, mean = -3.2 Wm^{-2}), and Southern Equatorial Africa (min = -3.8 Wm^{-2}, mean = -1.2 Wm^{-2}). This mirrors nitrate's radiative signal in HA14. The SLOW simulation exhibits smaller radiative impacts than FAST, with significant changes limited to South Asia (min = -7.7 Wm^{-2}, mean = -1.5 Wm-2) and Southern Equatorial Africa (min = -3.5 Wm^{-2}, mean = -0.7 Wm^{-2}). Figure 12 highlights the regionality of ammonium nitrate climate forcing and further demonstrates the significant differences between the FAST and SLOW simulations.

4 Conclusions and Discussion

A thermodynamic equilibrium nitrate scheme has been added to UKCA-mode and tested in the Met Office's Unified Model. In contrast to widely utilised 'instantaneous' thermodynamic equilibrium models, the UKCA nitrate scheme limits the rate at which ammonium nitrate ($NH_4 \cdot NO_3$) concentrations reach equilibrium using first-order condensation theory. Sensitivity tests

are performed to assess the sensitivity of $NH_4.NO_3$ concentrations to the nitric acid (HNO_3) uptake coefficient (γ in Eq. 7). Specifically, two values of γ are chosen to represent fast uptake rates ($\gamma = 0.193$; FAST) and slow uptake rates ($\gamma = 0.001$; SLOW) based on the range of γ measurements from the literature (e.g. Bauer *et al.*, 2004). While it is known that γ varies with aerosol composition, temperature, and relativity humidity (e.g. Vlasenko *et al.*, 2006), well-constrained values for HNO_3

695 uptake on common aerosol species (e.g. sulphate, organic carbon, black carbon) are at present lacking. As a first order sensitivity test, the HNO_3 uptake coefficient used in $NH_4.NO_3$ production is assumed to be globally invariant to aerosol composition (with the exception of mineral dust), temperature and relative humidity in FAST and SLOW. A third nitrate simulation in which $NH_4.NO_3$ reaches thermodynamic equilibrium instantaneously (INSTANT), is shown to produce near-identical results to FAST.

700

To help evaluate the sensitivity of $NH_4.NO_3$ concentrations to HNO_3 uptake coefficient, and the suitability of the FAST and SLOW uptake coefficients, a range of surface and satellite observations and comparable modelling studies have been compared to the UM simulations. Many robust results emerge from the simulations. Fine NO_3 concentrations are a factor of 2 greater in FAST than in SLOW on a global-mean basis, with associated increases to NH_4 concentrations in FAST. The largest differences

705 are over land regions in North America, Europe, South and East Asia, and Equatorial Africa. However, there are minimal differences between coarse NO_3 (associated with dust and sea-salt) concentrations in FAST and SLOW. Over many populous land regions (Europe, North America, East and South East Asia, and West and Equatorial Africa), seasonal near-surface $NH_4.NO_3$ concentrations are closely correlated with seasonal NH_3 emissions suggesting that NH_3 availability is the limiting factor controlling $NH_4.NO_3$ prevalence (Giannakis *et al.*, 2019). In the SLOW simulation, coarse NO_3 concentrations are of a

710 similar magnitude to fine NO_3 concentrations over many industrialised regions. Comparing the simulated concentrations to CASTNet observations (i.e. the US network), FAST better captures the spatial distribution of near-surface NO_3, NH_4, and HNO_3 concentrations but is positively biased, whereas SLOW better captures the magnitude of the concentrations. Total NO_3 concentrations over Europe are comparable between SLOW and EMEP observations but are a factor of 3-4 too high in FAST. Many of the biases in simulated NH_4 and NO_3 concentrations appear to be artefacts of biases in precursor gas (HNO_3 and NH_3)

715 concentrations. Significant AOD and TOA radiative flux impacts are mostly isolated to land regions with substantial $NH_4.NO_3$ burdens. On a global mean basis, the nitrate ERF is -0.17 Wm^{-2} in FAST and -0.07 Wm^{-2} in SLOW which mirrors the ratio of $NH_4.NO_3$ burdens in the two simulations.

Introducing a kinetic limitation on the rate at which $NH_4.NO_3$ concentrations reach equilibrium has minimal effect for $\gamma = $

720 0.193 (i.e. comparing FAST with INSTANT) but a significant effect equivalent to a halving for $\gamma = 0.001$ (i.e. comparing SLOW with FAST). In general, FAST exhibits better spatial correlation with observed nitrate concentrations while SLOW better resolves the magnitude of concentrations. Note though that there are many caveats associated with this study. Using a globally uniform value for the HNO_3 uptake coefficient (γ) obviates the dependence of γ on aerosol composition and relative humidity. A better parameterisation may instead utilise a volume-weighted γ depending on aerosol composition and ambient

725 relative humidity. Additionally, assuming the same value of γ for both HNO$_3$ and NH$_3$ is a pragmatic simplification owing to the dearth of γ measurements. For example, Benduhn *et al.* (2016) assume uptake coefficients of 0.2 and 0.1 for HNO$_3$ and NH$_3$ respectively. On another note, if γ is used to tune the NH$_4$·NO$_3$ concentrations to observations in future then existing biases in precursor gases (HNO$_3$ and NH$_3$), in terms of emissions and atmospheric processes, should first be evaluated and addressed. For instance, the curious surplus of simulated NH$_3$ at night at UK sites (Figure S10 in the Supplement) may be

730 rectified by imposing a diurnal cycle on NH$_3$ emissions based on number of daylight hours, as implemented by Park *et al.* (2004). Bian *et al.* (2017) also highlight the importance of accurately simulating NH$_3$ dissolution in cloud droplets, which may be oversimplified in the UM owing to the ubiquitous assumption of a cloud droplet pH of 5 in UKCA. This study has also highlighted a potential overestimate of NH$_3$ emissions in Europe in the CMIP6 emissions inventory, as also posited by Druge *et al.* (2019). An accurate NH$_3$ and NO$_x$ emissions inventory is vital for a proficient simulation of NH$_4$ and NO$_3$ concentrations.

735 HNO$_3$ concentrations also appear to be overestimated over the western US (Fig. 5) in these simulations, which may emanate from an oversimplification of heterogeneous N$_2$O$_5$ chemistry in UKCA Strattrop1.0, given that the uptake coefficient in that reaction is uniformly set to 0.1 (Archibald *et al.*, 2020).

The differences between the simulated and observed concentrations in this study (Figs 5-7) may be attributed to the use of

740 perpetual year-2000 conditions in these simulations; the coarse model resolution utilised here (N96); biases in HNO$_3$ and NH$_3$ emissions; deficiencies in the thermodynamic equilibrium approach; and due to the choice of a monotonic uptake coefficient. In particular, this study has shown that the HNO$_3$ uptake coefficient is an important parameter in the production of ammonium nitrate and assuming a monotonic value in climate models may be too simplified an approach given the high sensitivity of HNO$_3$ uptake to ambient aerosol composition. Future simulations would benefit from stronger observational constraints on the

745 HNO$_3$ and NH$_3$ uptake rates as a function of aerosol composition, relative humidity, and temperature, perhaps from targeted laboratory studies.

In a follow-on study, we aim to evaluate the nitrate scheme in high-resolution UM simulations for specific meteorological case-studies in a manner analogous to Gordon *et al.* (2018) but over a UK-based domain. Additionally, we will replace the

750 constant HNO$_3$ uptake coefficient in the new nitrate scheme with a volume-weighted value based on aerosol composition and relative humidity, and re-run the simulations using transient CMIP6-like atmosphere-only UM integrations. The next issue to address will be coupling NO$_3$ and NH$_4$ aerosol within the UKESM framework. At present, fixed nitrogen (NO$_y$ + NH$_x$) deposition to the land-surface model (JULES) in UKESM is applied using offline deposition fields from the input4MIPs database (see Sellar *et al.* (2020) for further details). Meanwhile, the ocean biogeochemistry module in UKESM (MEDUSA2;

755 Yool *et al.* (2003)) has a closed nitrogen budget thus obviating interactions with atmospheric nitrogen. With the addition of ammonium and nitrate aerosol to a future version of UKESM, we will aim to fully couple atmospheric fixed-nitrogen deposition with the land and ocean surfaces to permit a comprehensive closed-budget nitrogen cycle.

Atmospheric
Chemistry
and Physics
Discussions

760 In conclusion, the addition of ammonium and nitrate aerosol to UKCA-mode in the UM is step-change in aerosol-modelling capability in the UK and will increase confidence in future simulations of aerosol forcing and regional air pollution episodes. Additionally, nitrate concentrations have been shown to be highly sensitive to the nitric acid uptake rate, paving a way for climate models to reduce outstanding biases in ammonium nitrate concentrations.

Code Availability

Due to intellectual property rights restrictions, we cannot provide either the source code or documentation papers for the UM.
765 The Met Office Unified Model is available for use under licence. A number of research organisations and national meteorological services use the UM in collaboration with the Met Office to undertake basic atmospheric process research, produce forecasts, develop the UM code, and build and evaluate Earth system models. For further information on how to apply for a licence, see http://www.metoffice.gov.uk/research/modelling-systems/unified-model (last access: 16 April 2021). The nitrate scheme is now available on the 'trunk' (the Met Office's data repository) and is available for all future UM versions
770 since vn11.8 in UKCA mode setup 10.

Data Availability

The UM data used to produce the figures is available from the Centre of Environmental Data Analysis (CEDA) (http://dx.doi.org/10.5285/0613b74ecc574fa7b6ac8a22838c5f81; last accessed 12/05/2021) and if used should be cited accordingly: Jones, A.C.; Hill, A.; Remy, S.; Abraham, N.L.; Dalvi, M.; Hardacre, C.; Hewitt, A.J.; Johnson, B.; Mulcahy,
775 J.P.; Turnock, S. (2021): Exploring the sensitivity of atmospheric nitrate concentrations to nitric acid uptake rate using the Met Office's Unified Model: nitrate and nitric acid simulation data. NERC EDS Centre for Environmental Data Analysis, *date of citation*. https://catalogue.ceda.ac.uk/uuid/0613b74ecc574fa7b6ac8a22838c5f81

Competing Interests

The authors declare that they have no conflict of interest.

780 **Author contributions**

ACJ developed the nitrate scheme with assistance from AH, SR, NLA, MD, and AJH. ACJ performed the simulations with assistance from NLA and MD. ACJ, AH, CH, BJ, JM, and SR analysed the simulations and compared the results to observations. ACJ wrote the manuscript with assistance from all co-authors.

Atmospheric
Chemistry
and Physics
Discussions

800   **References**

Aas, W., Tsyro, S., Bieber, E., Bergström, R., Ceburnis, D., Ellermann, T., Fagerli, H., Frölich, M., Gehrig, R., Makkonen, U., Nemitz, E., Otjes, R., Perez, N., Perrino, C., Prévôt, A. S. H., Putaud, J.-P., Simpson, D., Spindler, G., Vana, M., and Yttri, K. E.: Lessons learnt from the first EMEP intensive measurement periods, Atmos. Chem. Phys., 12, 8073–8094, doi:10.5194/acp12-8073-2012, 2012.

805

Abdul-Razzak, H. and Ghan, S. J.: A parameterization of aerosol activation: 2. Multiple aerosol types, J. Geophys. Res.-Atmos., 105, 6837–6844, https://doi.org/10.1029/1999JD901161, 2000.

Ackermann, I. J., Hass, H., Memmesheimer, M., Ziegenbein, C., and Ebel, A.: The parameterization of the sulfate-nitrate

810   ammonia aerosol system in the long-range transport model EURAD, Meteorol. Atmos. Phys., 57, 101–114, 1995.

Ansari, A. S., and S. N. Pandis: Response of inorganic PM to precursor concentrations, Environ. Sci. Technol., 32, 2706–2714, 1998.

815   Archibald, A. T., O'Connor, F. M., Abraham, N. L., Archer-Nicholls, S., Chipperfield, M. P., Dalvi, M., Folberth, G. A.,
       Dennison, F., Dhomse, S. S., Griffiths, P. T., Hardacre, C., Hewitt, A. J., Hill, R. S., Johnson, C. E., Keeble, J., Köhler, M. O.,
       Morgenstern, O., Mulcahy, J. P., Ordóñez, C., Pope, R. J., Rumbold, S. T., Russo, M. R., Savage, N. H., Sellar, A., Stringer,
       M., Turnock, S. T., Wild, O., and Zeng, G.: Description and evaluation of the UKCA stratosphere–troposphere chemistry
       scheme (StratTrop vn 1.0) implemented in UKESM1, Geosci. Model Dev., 13, 1223–1266, https://doi.org/10.5194/gmd-13-
820   1223-2020, 2020.

       Atkinson, R.: Atmospheric Chemistry of VOCs and NOx, Atmos. Environ., 34, 2063–2101, https://doi.org/10.1016/S1352-
       2310(99)00460-4, 2000.

825   Ballard, S.S., Browder, J.S., and Ebersole, J.F.: Refractive index of special crystals and certain glasses, in American Institute
       of Physics Handbook, 3rd ed., McGraw-Hill, New York, 1972.

       Bauer, S. E., Balkanski, Y., Schulz, M., Hauglustaine, D. A., and Dentener, F.: Global modeling of heterogeneous chemistry
       on mineral aerosol surfaces: influence on tropospheric ozone chemistry and comparison to observations, J. Geophys. Res.,
830   109, D02304, doi:10.1029/2003JD003868, 2004.

       Bauer, S. E., Koch, D., Unger, N., Metzger, S. M., Shindell, D. T., and Streets, D. G.: Nitrate aerosols today and in 2030: a
       global simulation including aerosols and tropospheric ozone, Atmos. Chem. Phys., 7, 5043–5059, doi:10.5194/acp-7-5043-
       2007, 2007.

835
       Bauer, S. E., Tsigaridis, K., and Miller, R.: Significant atmospheric aerosol pollution caused by world food cultivation,
       Geophys. Res. Lett., 43, 5394–5400, doi:10.1002/2016GL068354., 2016.

       Bellouin, N., Boucher, O., Haywood, J., Johnson, C., Jones, A., Rae, J., and Woodward, S.: Improved representation of aerosols
840   for HadGEM2, Hadley Centre technical note 73, Hadley Centre, Met Office, Exeter, UK, available at:
       http://www.metoffice.gov.uk/media/pdf/8/f/HCTN_73.pdf, 42 pp., 2007.

       Bellouin, N., Rae, J., Jones, A., Johnson, C., Haywood, J., and Boucher, O.: Aerosol forcing in the Climate Model
       Intercomparison Project (CMIP5) simulations by HadGEM2-ES and the role of ammonium nitrate, J. Geophys. Res.-Atmos.,
845   116, D20206, https://doi.org/10.1029/2011jd016074, 2011.

Bellouin, N., Mann, G. W., Woodhouse, M. T., Johnson, C., Carslaw, K. S., and Dalvi, M.: Impact of the modal aerosol scheme GLOMAP-mode on aerosol forcing in the Hadley Centre Global Environmental Model, Atmos. Chem. Phys., 13, 3027–3044, https://doi.org/10.5194/acp-13-3027-2013, 2013.

850

Bellouin, N., Quaas, J., Gryspeerdt, E., Kinne, S., Stier, P., WatsonParris, D., Boucher, O., Carslaw, K., Christensen, M., Daniau, A.-L., Dufresne, J.-L., Feingold, G., Fiedler, S., Forster, P., Gettelman, A., Haywood, J., Lohmann, U., Malavelle, F., Mauritsen, T., McCoy, D., Myhre, G., Mülmenstädt, J., Neubauer, D., Possner, A., Rugenstein, M., Sato, Y., Schulz, M., Schwartz, S., Sourdeval, O., Storelvmo, T., Toll, V., Winker, D., and Stevens, B.: Bounding global aerosol radiative forcing

855   of climate change, Rev. Geophys., 58, e2019RG000660, https://doi.org/10.1029/2019RG000660, 2020.

Benduhn, F., Mann, G. W., Pringle, K. J., Topping, D. O., McFiggans, G., and Carslaw, K. S.: Size-resolved simulations of the aerosol inorganic composition with the new hybrid dissolution solver HyDiS-1.0 – Description, evaluation and first global modelling results, Geosci. Model Dev., 9, 3875–3906, doi:10.5194/gmd-9-3875-2016, 2016.

860

Bian, H., Chin, M., Hauglustaine, D. A., Schulz, M., Myhre, G., Bauer, S. E., Lund, M. T., Karydis, V. A., Kucsera, T. L., Pan, X., Pozzer, A., Skeie, R. B., Steenrod, S. D., Sudo, K., Tsigaridis, K., Tsimpidi, A. P., and Tsyro, S. G.: Investigation of global particulate nitrate from the AeroCom phase III experiment, Atmos. Chem. Phys., 17, 12911–12940, https://doi.org/10.5194/acp-17-12911-2017, 2017.

865

Boutle, I. A., Abel, S. J., Hill, P. G., and Morcrette, C. J.: Spatial variability of liquid cloud and rain: observations and microphysical effects, Q. J. Roy. Meteorol. Soc., 140, 583–594, https://doi.org/10.1002/qj.2140, 2014

Bouwman, A. F., Lee, D. S., Asman, W. A. H., Dentener, F. J., Van Der Hoek, K. W., and Olivier, J. G. J.: A Global High-

870   Resolution Emission Inventory for Ammonia, Global Biogeochem. Cy., 11, 561–587, https://doi.org/10.1029/97GB02266, 1997.

Buchard, V., Randles, C. A., da Silva, A. M., Darmenov, A., Colarco, P. R., Govindaraju, R., Ferrare, R., Hair, J., Beyersdorf, A. J., Ziemba, L. D., Yu, H., Buchard, V., Randles, C. A., Silva, A. M. da, Darmenov, A., Colarco, P. R., Govindaraju, R.,

875   Ferrare, R., Hair, J., Beyersdorf, A. J., Ziemba, L. D., and Yu, H.: The MERRA-2 Aerosol Reanalysis, 1980 Onward. Part II: Evaluation and Case Studies, J. Clim., 30, 6851–6872, https://doi.org/10.1175/JCLI-D-16-0613.1, 2017.

Carn, S. A., Fioletov, V. E., McLinden, C. A., Li, C., and Krotkov, N. A.: A decade of global volcanic SO2 emissions measured from space, Sci. Rep., 7, 44095, https://doi.org/10.1038/srep44095, 2017.

880

Atmospheric
Chemistry
and Physics
Discussions

Cleaver, B., Rhodes, E., and Ubbelohde, A. R.: Studies of phase transformations in nitrates and nitrites I. Changes in ultra-violet absorption spectra on melting, Proc. R. Soc. London, 276, 437-453, https://doi.org/10.1098/rspa.1963.0217, 1963.

885 Cotterell, M. I., Willoughby, R. E., Bzdek, B. R., Orr-Ewing, A. J., and Reid, J. P.: A complete parameterisation of the relative humidity and wavelength dependence of the refractive index of hygroscopic inorganic aerosol particles, Atmos. Chem. Phys., 17, 9837–9851, https://doi.org/10.5194/acp-17-9837-2017, 2017.

Crutzen, P. J.: The influence of nitrogen oxides on the atmospheric ozone content, Q. J. Roy. Meteorol. Soc., 96, 320–325, doi:10.1002/qj.49709640815, 1970.

890

Department for Environment, Food and Rural Affairs (DEFRA): Report: Fine Particulate Matter (PM2.5) in the United Kingdom, Available here: https://uk-air.defra.gov.uk/library/reports?report_id=727, pp. 203, Published: 14/12/2012, DEFRA, London, UK, 2012.

895 Drugé, T., Nabat, P., Mallet, M., and Somot, S.: Model simulation of ammonium and nitrate aerosols distribution in the Euro-Mediterranean region and their radiative and climatic effects over 1979–2016, Atmos. Chem. Phys., 19, 3707–3731, https://doi.org/10.5194/acp-19-3707-2019, 2019.

Fairlie, T. D., Jacob, D. J., Dibb, J. E., Alexander, B., Avery, M. A., van Donkelaar, A., and Zhang, L.: Impact of mineral dust 900 on nitrate, sulfate, and ozone in transpacific Asian pollution plumes, Atmos. Chem. Phys., 10, 3999–4012, doi:10.5194/acp-10-3999-2010, 2010.

Feng, Y. and Penner, J. E.: Global modeling of nitrate and ammonium: Interaction of aerosols and tropospheric chemistry, J. Geophys. Res.-Atmos., 112, D01304, https://doi.org/10.1029/2005jd006404, 2007.

905

Feng, L., Smith, S. J., Braun, C., Crippa, M., Gidden, M. J., Hoesly, R., Klimont, Z., van Marle, M., van den Berg, M., and van der Werf, G. R.: The generation of gridded emissions data for CMIP6, Geosci. Model Dev., 13, 461–482, https://doi.org/10.5194/gmd-13-461-2020, 2020

910 Finkelstein, P., Ellestad, T., Clarke, J., Meyers, T., Schwede, D., Hebert, E., and Neal, J.: Ozone and sulfur dioxide dry deposition to forests: Observations and model evaluation, J. Geophys. Res.-Atmos, 105, 15, 365–377, https://doi.org/10.1029/2000JD900185, 2000.

Fortems-Cheiney, A., Dufour, G., Hamaoui-Laguel, L., Foret, G., Siour, G., Van Damme, M., Meleux, F., Coheur, P.-F.,
915   Clerbaux, C., Clarisse, L., Favez, O., Wallasch, M., and Beekmann, M.: Unaccounted variability in NH3 agricultural sources
       detected by IASI contributing to European spring haze episode, Geophys. Res. Lett., 43, 5475–
       5482, https://doi.org/10.1002/2016GL069361, 2016.

Fuchs, N. A. and Sutugin, A. G.: Highly Dispersed Aerosols, Butterworth-Heinemann, Newton, Mass., USA, 105, 1970.
920

Gerber, H. E.: Relative-humidity parameterization of the Navy Aerosol Model (NAM), NRL Report 8956, Naval Research
       Laboratory, Washington, DC, 1985.

Giannakis, E., Kushta, J., Bruggeman, A., and Lelieveld, J.: Costs and benefits of agricultural ammonia emission abatement
925   options for compliance with European air quality regulations, Environ. Sci. Eur., 31:93, https://doi.org/10.1186/s12302-019-
       0275-0, 2019.

Giannakopoulos, C., Chipperfield, T., Law, K., and Pyle, J.: Validation and intercomparison of wet and dry deposition schemes
       using Pb-210 in a global three-dimensional off-line chemical transport model, J. Geophys. Res., 104, 23761–23784, 1999.
930
Giorgi, F.: Climate change hot-spots, Geophys. Res. Lett., 33, L08707, https://doi.org/10.1029/2006GL025734, 2006.

Gordon, H., Field, P. R., Abel, S. J., Dalvi, M., Grosvenor, D. P., Hill, A. A., Johnson, B. T., Miltenberger, A. K., Yoshioka,
       M., and Carslaw, K. S.: Large simulated radiative effects of smoke in the south-east Atlantic, Atmos. Chem. Phys., 18, 15261–
935   15289, https://doi.org/10.5194/acp-18-15261-2018, 2018.

Gosse, S. F., Wang, M., Labrie, D., and Chylek, P.: Imaginary part of the refractive index of sulfates and nitrates in the 0.7–
       2.6 µm spectral region, Appl. Opt., 36, 16, 3622–3634, 1997.

940   Granier, C., Bessagnet, B., Bond, T., D'Angiola, A., Denier van der Gon, H., Frost, G. J., Heil, A., Kaiser, J. W., Kinne, S.,
       Klimont, Z., Kloster, S., Lamarque, J.-F., Liousse, C., Masui, T., Meleux, F., Mieville, A., Ohara, T., Raut, J.-C., Riahi, K.,
       Schultz, M. G., Smith, S. J., Thompson, A., van Aardenne, J., van der Werf, G. R., and van Vuuren, D. P.: Evolution of
       anthropogenic and biomass burning emissions of air pollutants at global and regional scales during the 1980–2010 period,
       Clim. Change, 109, 163–190, https://doi.org/10.1007/s10584-011-0154-1, 2011.
945

Hardacre, C., Mulcahy, J. P., Pope, R., Jones, C. G., Rumbold, S. R., Li, C., and Turnock, S. T.: Evaluation of SO2, SO4(2-) and an updated SO2 dry deposition parameterization in UKESM1, Atmos. Chem. Phys. Discuss., https://doi.org/10.5194/acp-2021-238

950   Hauglustaine, D. A., Balkanski, Y., and Schulz, M.: A global model simulation of present and future nitrate aerosols and their direct radiative forcing of climate, Atmos. Chem. Phys., 14, 11031– 11063, https://doi.org/10.5194/acp-14-11031-2014, 2014.

Hemmings, J., and Savage, N.: An Initial Evaluation of the GLOMAP-mode Aerosol Scheme for UK Air-Quality Forecasting with AQUM, Met Office Weather Science Technical Report No. 632, August 2018, pp. 70, Available here:
955   https://www.metoffice.gov.uk/research/library-and-archive/publications/science/weather-science-technical-reports,   Met Office, Exeter, UK, 2018.

Hoesly, R. M., Smith, S. J., Feng, L., Klimont, Z., Janssens-Maenhout, G., Pitkanen, T., Seibert, J. J., Vu, L., Andres, R. J., Bolt, R. M., Bond, T. C., Dawidowski, L., Kholod, N., Kurokawa, J.-I., Li, M., Liu, L., Lu, Z., Moura, M. C. P., O'Rourke, P.
960   R., and Zhang, Q.: Historical (1750–2014) anthropogenic emissions of reactive gases and aerosols from the Community Emissions Data System (CEDS), Geosci. Model Dev., 11, 369–408, https://doi.org/10.5194/gmd-11-369-2018, 2018.

Hsu, N. C., Jeong, M.-J., Bettenhausen, C., Sayer, A. M., Hansell, R., Seftor, C. S., Huang, J., and Tsay S.-C.: Enhanced Deep Blue aerosol retrieval algorithm: The second generation, J. Geophys. Res.-Atmos., 118, 9296–9315,
965   https://doi.org/10.1002/jgrd.50712, 2013.

Ivlev, L. S. and Popova, S. I.: Optical constants of substances of atmospheric aerosol, Sov. Phys. J., 15, 703–707, https://doi.org/10.1007/BF00893039, 1972.

970   Jacobson, M.: Numerical techniques to solve condensational and dissolutional growth equations when growth is coupled to reversible aqueous reactions, Aerosol Sci. Technol., 27, 491–498, doi:10.1080/02786829708965489,1997.

Jacobson, M. Z.: Isolating nitrated and aromatic aerosols and nitrated aromatic gases as sources of ultraviolet light absorption, J. Geophys. Res., 104, 3527–3542, https://doi.org/10.1029/1998JD100054, 1999.
975

Jarzembski, M. A., Norman, M. L., Fuller, K. A., Srivastava, V., and Cutten, D. R.: Complex refractive index of ammonium nitrate in the 2–20 μm spectral range, Appl. Optics, 42, 922–930, https://doi.org/10.1364/AO.42.000922, 2003.

Jimenez, J. L., Canagaratna, M. R., Donahue, N. M., Prevot, A. S. H., Zhang, Q., Kroll, J. H., DeCarlo, P. F., Allan, J. D., Coe,
980 H., Ng, N. L., Aiken, A. C., Docherty, K. S., Ulbrich, I. M., Grieshop, A. P., Robinson, A. L., Duplissy, J., Smith, J. D., Wilson,
K. R., Lanz, V. A., Hueglin, C., Sun, Y. L., Tian, J., Laaksonen, A., Raatikainen, T., Rautiainen, J., Vaattovaara, P., Ehn, M.,
Kulmala, M., Tomlinson, J. M., Collins, D. R., Cubison, M. J., Dunlea, E. J., Huffman, J. A., Onasch, T. B., Alfarra, M. R.,
Williams, P. I., Bower, K., Kondo, Y., Schneider, J., Drewnick, F., Borrmann, S., Weimer, S., Demerjian, K., Salcedo, D.,
Cottrell, L., Griffin, R., Takami, A., Miyoshi, T., Hatakeyama, S., Shimono, A., Sun, J. Y., Zhang, Y. M., Dzepina, K., Kimmel,
985 J. R., Sueper, D., Jayne, J. T., Herndon, S. C., Trimborn, A. M., Williams, L. R., Wood, E. C., Middlebrook, A. M., Kolb, C.
E., Baltensperger, U., and Worsnop, D. R.: Evolution of organic aerosols in the atmosphere, Science, 326, 5959, 1525–1529,
doi:10.1126/science.1180353, 2009.

Khairoutdinov, M. F. and Kogan, Y. L.: A new cloud physics parameterization in a large-eddy simulation model of marine
990 stratocumulus, Mon. Wea. Rev., 128, 229–243, https://doi.org/10.1175/1520-0493(2000)128<0229:ANCPPI>2.0.CO;2, 2000.

Kucera, V., and Fitz, S.: Direct and indirect air pollution effects on materials including cultural monuments, Water Air Soil
Pollut., 85, pp. 153-165, https://doi.org/10.1007/BF00483697, 1995.

995 Lelieveld, J., Evans, J. S., Fnais, M., Giannadaki, D., and Pozzer, A.: The contribution of outdoor air pollution sources to
premature mortality on a global scale, Nature, 525, 367–371, doi:10.1038/nature15371, 2015.

Levy, R. C., Mattoo, S., Munchak, L. A., Remer, L. A., Sayer, A. M., Patadia, F., and Hsu, N. C.: The Collection 6 MODIS
aerosol products over land and ocean, Atmos. Meas. Tech., 6, 2989–3034, https://doi.org/10.5194/amt-6-2989-2013, 2013.
1000
Li, W. J. and Shao, L. Y.: Observation of nitrate coatings on atmospheric mineral dust particles, Atmos. Chem. Phys., 9, 1863–
1871, doi:10.5194/acp-9-1863-2009, 2009.

Li, Y., Schichtel, B. A., Walker, J. T., Schwede, D. B., Chen, X., Lehmann, C. M. B., Puchalski, M. A., Gay, D. A., and Collett,
1005 J. L.: Increasing importance of deposition of reduced nitrogen in the United States, P. Natl. Acad. Sci. USA, 113, 5874–5879,
doi:10.1073/pnas.1525736113, 2016.

Liao, H., Adams, P. J., Chung, S. H., Seinfeld, J. H., Mickley, L. J., and Jacob, D. J.: Interactions between tropospheric
chemistry and aerosols in a unified general circulation model, J. Geophys. Res., 108, 4001, doi:10.1029/2001JD001260, 2003.
1010

Lovett, G. M., Tear, T. H., Evers, D. C., Findlay, S. E. G., Cosby, B. J., Dunscomb, J. K., Driscoll, C. T., and Weathers, K. C.: Effects of air pollution on ecosystems and biological diversity in the eastern United States, Ann. N. Y. Acad. Sci., 1162, 99-135, doi:10.1111/j.1749-6632.2009.04153.x, 2009.

1015   Makar, P. A., Wiebe, H. A., Staebler, R. M., Li, S.-M., and Anlauf, K.: Measurement and modelling of particle nitrate formation, J. Geophys. Res.-Atmos., 103, D11, 13 095–13 110, https://doi.org/10.1029/98JD00978, 1998.

Mann, G. W., Carslaw, K. S., Spracklen, D. V., Ridley, D. A., Mankte low, P. T., Chipperfield, M. P., Pickering, S. J., and Johnson, C. E.: Description and evaluation of GLOMAP-mode: a modal global aerosol microphysics mo del for the UKCA

1020   composition-climate model, Geosci. Model Dev., 3, 519–551, https://doi.org/10.5194/gmd-3-519-2010, 2010.

Manners, J., Edwards, J. M., Hill, P., and Thelen, J.-C.: SOCRATES (Suite Of Community RAdiative Transfer codes based on Edwards and Slingo) Technical Guide, Met Office, UK, available at: https://code.metoffice.gov.uk/trac/socrates (last access: 25 October 2017), 2015.

1025

McDuffie, E. E., Smith, S. J., O'Rourke, P., Tibrewal, K., Venkataraman, C., Marais, E. A., Zheng, B., Crippa, M., Brauer, M., and Martin, R. V.: A global anthropogenic emission inventory of atmospheric pollutants from sector- and fuel-specific sources (1970–2017): an application of the Community Emissions Data System (CEDS), Earth Syst. Sci. Data, 12, 3413–3442, https://doi.org/10.5194/essd-12-3413-2020, 2020.

1030

Metzger, S., Dentener, F., Pandis, S., and Lelieveld, J.: Gas/aerosol partitioning: 1. A computationally efficient model, J. Geophys. Res., 107, D164312, https://doi.org/10.1029/2001JD001102, 2002.

Monks, P. S., Granier, C., Fuzzi, S., Stohl, A., Williams, M. L., Akimoto, H., Amann, M., Baklanov, A., Baltensperger, U.,
1035   Bey, I., Blake, N., Blake, R. S., Carslaw, K., Cooper, O. R., Dentener, F., Fowler, D., Fragkou, E., Frost, G. J., Generoso, S., Ginoux, P., Grewe, V., Guenther, A., Hansson, H. C., Henne, S., Hjorth, J., Hofzumahaus, A., Huntrieser, H., Isaksen, I. S. A., Jenkin, M. E., Kaiser, J., Kanakidou, M., Klimont, Z., Kulmala, M., Laj, P., Lawrence, M. G., Lee, J. D., Liousse, C., Maione, M., McFiggans, G., Metzger, A., Mieville, A., Moussiopoulos, N., Orlando, J. J., O'Dowd, C. D., Palmer, P. I., Parrish, D. D., Petzold, A., Platt, U., Poeschl, U., Prevot, A. S. H., Reeves, C. E., Reimann, S., Rudich, Y., Sellegri, K.,
1040   Steinbrecher, R., Simpson, D., ten Brink, H., Theloke, J., van der Werf, G. R., Vautard, R., Vestreng, V., Vlachokostas, C., and von Glasow, R.: Atmospheric composition change – global and regional air quality, Atmos. Environ., 43, 5268–5350, doi:10.1016/j.atmosenv.2009.08.021, 2009.

Atmospheric
Chemistry
and Physics
Discussions

Open Access

EGU

Mozurkewich, M.: The dissociation constant of ammonium nitrate and its dependence on temperature, relative humidity and
1045   particle size, Atmos. Environ. A-Gen., 27, 261–270, 1993.

Mulcahy, J. P., Jones, C., Sellar, A., Johnson, B., Boutle, I. A., Jones, A., Andrews, T., Rumbold, S. T., Mollard, J., Bellouin,
N., Johnson, C. E., Williams, K. D., Grosvenor, D. P., and McCoy, D. T.: Improved Aerosol Processes and Effective Radiative
Forcing in HadGEM3 and UKESM1, J. Adv. Model. Earth Syst., 10, 2786–2805, https://doi.org/10.1029/2018MS001464,
1050   2018.

Mulcahy, J. P., Johnson, C., Jones, C. G., Povey, A. C., Scott, C. E., Sellar, A., Turnock, S. T., Woodhouse, M. T., Abraham,
N. L., Andrews, M. B., Bellouin, N., Browse, J., Carslaw, K. S., Dalvi, M., Folberth, G. A., Glover, M., Grosvenor, D. P.,
Hardacre, C., Hill, R., Johnson, B., Jones, A., Kipling, Z., Mann, G., Mollard, J., O'Connor, F. M., Palmiéri, J., Reddington,
1055   C., Rumbold, S. T., Richardson, M., Schutgens, N. A. J., Stier, P., Stringer, M., Tang, Y., Walton, J., Woodward, S., and Yool,
A.: Description and evaluation of aerosol in UKESM1 and HadGEM3-GC3.1 CMIP6 historical simulations, Geosci. Model
Dev., 13, 6383–6423, https://doi.org/10.5194/gmd-13-6383-2020, 2020.

Myhre, G., Grini, A., and Metzger, S.: Modelling of nitrate and ammonium-containing aerosols in presence of sea salt, Atmos.
1060   Chem. Phys., 6, 4809–4821, http://www.atmos-chem-phys.net/6/4809/2006/, 2006.

Myhre, G., Samset, B. H., Schulz, M., Balkanski, Y., Bauer, S., Berntsen, T. K., Bian, H., Bellouin, N., Chin, M., Diehl, T.,
Easter, R. C., Feichter, J., Ghan, S. J., Hauglustaine, D., Iversen, T., Kinne, S., Kirkevåg, A., Lamarque, J.-F., Lin, G., Liu, X.,
Lund, M. T., Luo, G., Ma, X., van Noije, T., Penner, J. E., Rasch, P. J., Ruiz, A., Seland, Ø., Skeie, R. B., Stier, P., Takemura,
1065   T., Tsigaridis, K., Wang, P., Wang, Z., Xu, L., Yu, H., Yu, F., Yoon, J.-H., Zhang, K., Zhang, H., and Zhou, C.: Radiative
forcing of the direct aerosol effect from AeroCom Phase II simulations, Atmos. Chem. Phys., 13, 1853–1877,
https://doi.org/10.5194/acp13-1853-2013, 2013.

Nenes, A., Pandis, S. N., and Pilinis, C.: ISORROPIA: A new thermodynamic equilibrium model for multiphase
1070   multicomponent inorganic aerosols, Aquat. Geochem., 4, 123–152, https://doi.org/10.1023/A:1009604003981, 1998.

O'Connor, F. M., Johnson, C. E., Morgenstern, O., Abraham, N. L., Braesicke, P., Dalvi, M., Folberth, G. A., Sanderson, M.
G., Telford, P. J., Voulgarakis, A., Young, P. J., Zeng, G., Collins, W. J., and Pyle, J. A.: Evaluation of the new UKCA climate-
composition model – Part 2: The Troposphere, Geosci. Model Dev., 7, 41–91, https://doi.org/10.5194/gmd-7-41-2014, 2014.

1075

Palik, E. D.; Khanna, R. Sodium Nitrate (NaNO3). In Handbook of Optical Constants; Palik, E. D., Ed.; Academic Press: New
York, 1998; Vol. 3, p 871, 1998.

Park, R. J., Jacob, D. J., Field, B. D., Yantosca, R. M., and Chin, M.: Natural and transboundary pollution influences on sulfate-
1080   nitrate-ammonium aerosols in the United States: Implications for policy, J. Geophys. Res., 109, D15204,
doi:10.1029/2003JD004473, 2004.

Paulot, F., Ginoux, P., Cooke, W. F., Donner, L. J., Fan, S., Lin, M.-Y., Mao, J., Naik, V., and Horowitz, L. W.: Sensitivity of
nitrate aerosols to ammonia emissions and to nitrate chemistry: implications for present and future nitrate optical depth, Atmos.
1085   Chem. Phys., 16, 1459–1477, https://doi.org/10.5194/acp16-1459-2016, 2016.

Putaud, J. P., Raes, F., Van Dingenen, R., Bruggemann, E., Fac- ¨chini, M. C., Decesari, S., Fuzzi, S., Gehrig, R., Huglin, C.,
Laj, ¨ P., Lorbeer, G., Maenhaut, W., Mihalopoulos, N., Muller, K., ¨ Querol, X., Rodriguez, S., Schneider, J., Spindler, G.,
ten Brink, H., Tørseth, K., and Wiedensohler, A.: A European aerosol phenomenology 2: chemical characteristics of particulate
1090   matter at kerbside, urban, rural and background sites in Europe, Atmos. Environ., 38, 2579–2595, 2004

Randles, C. A., da Silva, A. M., Buchard, V., Colarco, P. R., Darmenov, A., Govindaraju, R., Smirnov, A., Holben, B., Ferrare,
R., Hair, J., Shinozuka, Y., Flynn, C. J., Randles, C. A., Silva, A. M. da, Buchard, V., Colarco, P. R., Darmenov, A.,
Govindaraju, R., Smirnov, A., Holben, B., Ferrare, R., Hair, J., Shinozuka, Y., and Flynn, C. J.: The MERRA-2 Aerosol
1095   Reanalysis, 1980 Onward. Part I: System Description and Data Assimilation Evaluation, J. Clim., 30, 6823–6850,
https://doi.org/10.1175/JCLI-D16-0609.1, 2017.

Reddington, C. L., Carslaw, K. S., Stier, P., Schutgens, N., Coe, H., Liu, D., Allan, J., Browse, J., Pringle, K. J., Lee, L. A.,
Yoshioka, M., Johnson, J. S., Regayre, L. A., Spracklen, D. V., Mann, G. W., Clarke, A., Hermann, M., Henning, S., Wex, H.,
1100   Kristensen, T. B., Leaitch, W. R., Pöschl, U., Rose, D., Andreae, M. O., Schmale, J., Kondo, Y., Oshima, N., Schwarz, J. P.,
Nenes, A., Anderson, B., Roberts, G. C., Snider, J. R., Leck, C., Quinn, P. K., Chi, X., Ding, A., Jimenez, J. L., and Zhang,
Q.: The global aerosol synthesis and science project (GASSP): Measurements and modeling to reduce uncertainty, B. Am.
Meteorol. Soc., 98, 1857–1877, https://doi.org/10.1175/BAMS-D-15-00317.1, 2017.

1105   Rémy, S., Kipling, Z., Flemming, J., Boucher, O., Nabat, P., Michou, M., Bozzo, A., Ades, M., Huijnen, V., Benedetti, A.,
Engelen, R., Peuch, V.-H., and Morcrette, J.-J.: Description and evaluation of the tropospheric aerosol scheme in the European
Centre for Medium-Range Weather Forecasts (ECMWF) Integrated Forecasting System (IFS-AER, cycle 45R1), Geosci.
Model Dev., 12, 4627–4659, https://doi.org/10.5194/gmd-12-4627-2019, 2019.

1110   Sander, S. P., Abbatt, J., Barker, J. R., Burkholder, J. B., Friedl, R. R., Golden, D. M., Huie, R. E., Kolb, C. E., Kurylo, M. J., Moortgat, G. K., Orkin, V. L., and Wine, P. H.: Chemical Kinetics and Photochemical Data for Use in Atmospheric Studies, Evaluation No. 17, JPL Publication 10-6, Jet Propulsion Laboratory, Pasadena, 2011.

Savage, N. H., Agnew, P., Davis, L. S., Ordóñez, C., Thorpe, R., Johnson, C. E., O'Connor, F. M., and Dalvi, M.: Air quality
1115   modelling using the Met Office Unified Model (AQUM OS24-26): model description and initial evaluation, Geosci. Model Dev., 6, 353–372, doi:10.5194/gmd-6-353-2013, 2013.

Schwartz, S. E.: Mass transport considerations pertinent to aqueous phase reactions of gases in liquid-water clouds, in: Chemistry of Multiphase Atmospheric Systems, edited by: Jaeschke, W., 415–471, Springer, New York, 1986.
1120
Seinfeld, J. H. and Pandis, S. N.: Atmospheric Chemistry and Physics: From Air Pollution to Climate Change, John, Wiley & Sons, Inc., 1998.

Sellar, A., Jones, C. G., Mulcahy, J. P., Tang, Y., Yool, A., Wiltshire, A., O'Connor, F. M., Stringer, M., Hill, R., Palmieri, J.,
1125   Woodward, S., de Mora, L., Kuhlbrodt, T., Rumbold, S., Kelley, D. I., Ellis, R., Johnson, C. E., Walton, J., Abraham, N. L., Andrews, M. B., Andrews, T., Archibald, A. T., Berthou, S., Burke, E., Blockley, E., Carslaw, K., Dalvi, M., Edwards, J., Folberth, G. A., Gedney, N., Griffiths, P. T., Harper, A. B., Hendry, M. A., Hewitt, A. J., Johnson, B., Jones, A., Jones, C. D., Keeble, J., Liddicoat, S., Morgenstern, O., Parker, R. J., Predoi, V., Robertson, E., Siahaan, A., Smith, R. S., Swaminathan, R., Woodhouse, M., Zeng, G., and Zerroukat, M.: UKESM1: Description and evaluation of the UK Earth System Model, J.
1130   Adv. Model. Earth Syst., https://doi.org/10.1029/2019MS001739, 2019.

Sellar, A., Walton, J., Jones, C. G., Wood, R., Abraham, N. L., Andrejczuk, M., Andrews, M. B., Andrews, T., Archibald, A. T., Dyson, H., Elkington, M., Ellis, R., Florek, P., Good, P., Gohar, L., Haddad, S., Hardiman, S. C., Hogan, E., Iwi, A., Jones, C. D., Johnson, B., Kelley, D. I., Kettleborough, J., Knight, J. R., Köhler, M. 5 O., Kuhlbrodt, T., Liddicoat, S., Linova-
1135   Pavlova, I., Mizielinski, M. S., Morgenstern, O., Mulcahy, J., Neininger, E., O'Connor, F. M., Petrie, R., Ridley, J., Rioual, J.-C., Roberts, M., Robertson, E., Rumbold, S., Seddon, J., Shepherd, H., Shim, S., Stephens, A., Teixeira, J. C., Tang, Y., Williams, J., and Wiltshire, A.: Implementation of UK Earth system models for CMIP6, J. Adv. Model. Earth Syst., 12, e2019MS001946. https://doi.org/10.1029/2019MS001946, 2020.

1140   Smith, C., Hill, A. K., and Torrente-Murciano, L.: Current and future role of Haber–Bosch ammonia in a carbon-free energy landscape, Energy Environ. Sci., doi: 10.1039/c9ee02873k, 13, 331, 2020.

Telford, P. J., Abraham, N. L., Archibald, A. T., Braesicke, P., Dalvi, M., Morgenstern, O., O'Connor, F. M., Richards, N. A. D., and Pyle, J. A.: Implementation of the Fast-JX Photolysis scheme (v6.4) into the UKCA component of the MetUM chemistry-climate model (v7.3), Geosci. Model Dev., 6, 161–177, https://doi.org/10.5194/gmd-6-161-2013, 2013.

Torseth, K., Aas, W., Breivik, K., Fjaeraa, A. M., Fiebig, M., Hjellbrekke, A. G., Myhre, C. L., Solberg, S., and Yttri, K. E.: Introduction to the European Monitoring and Evaluation Programme (EMEP) and observed atmospheric composition change during 1972-2009, Atmos. Chem. Phys., 12, 5447–5481, https://doi.org/10.5194/acp-12-5447-2012, 2012.

Turnock, S. T., Allen, R. J., Andrews, M., Bauer, S. E., Deushi, M., Emmons, L., Good, P., Horowitz, L., John, J. G., Michou, M., Nabat, P., Naik, V., Neubauer, D., O'Connor, F. M., Olivié, D., Oshima, N., Schulz, M., Sellar, A., Shim, S., Takemura, T., Tilmes, S., Tsigaridis, K., Wu, T., and Zhang, J.: Historical and future changes in air pollutants from CMIP6 models, Atmos. Chem. Phys., 20, 14547–14579, https://doi.org/10.5194/acp-20-14547-2020, 2020.

Twigg, M. M., Ilyinskaya, E., Beccaceci, S., Green, D. C., Jones, M. R., Langford, B., Leeson, S. R., Lingard, J. J. N., Pereira, G. M., Carter, H., Poskitt, J., Richter, A., Ritchie, S., Simmons, I., Smith, R. I., Tang, Y. S., Van Dijk, N., Vincent, K., Nemitz, E., Vieno, M., and Braban, C. F.: Impacts of the 2014–2015 Holuhraun eruption on the UK atmosphere, Atmos. Chem. Phys., 16, 11415–11431, https://doi.org/10.5194/acp-16-11415-2016, 2016.

van Marle, M. J. E., Kloster, S., Magi, B. I., Marlon, J. R., Daniau, A.-L., Field, R. D., Arneth, A., Forrest, M., Hantson, S., Kehrwald, N. M., Knorr, W., Lasslop, G., Li, F., Mangeon, S., Yue, C., Kaiser, J. W., and van der Werf, G. R.: Historic global biomass burning emissions for CMIP6 (BB4CMIP) based on merging satellite observations with proxies and fire models (1750–2015), Geosci. Model Dev., 10, 3329–3357, https://doi.org/10.5194/gmd-10-3329-2017, 2017.

Vlasenko, A., Sjogren, S., Weingartner, E., Stemmler, K., Gaggeler, H. W., and Ammann, M.: Effect of humidity on nitric acid uptake to mineral dust aerosol particles, Atmos. Chem. Phys., 6, 2147– 2160, doi:10.5194/acp-6-2147-2006, 2006.

Vinken, G. C. M., Boersma, K. F., Maasakkers, J. D., Adon, M., and Martin, R. V.: Worldwide biogenic soil NOx emissions inferred from OMI NO2 observations, Atmos. Chem. Phys., 14, 10363– 10381, doi:10.5194/acp-14-10363-2014, 2014.

Walters, D., Baran, A. J., Boutle, I., Brooks, M., Earnshaw, P., Edwards, J., Furtado, K., Hill, P., Lock, A., Manners, J., Morcrette, C., Mulcahy, J., Sanchez, C., Smith, C., Stratton, R., Tennant, W., Tomassini, L., Van Weverberg, K., Vosper, S., Willett, M., Browse, J., Bushell, A., Carslaw, K., Dalvi, M., Essery, R., Gedney, N., Hardiman, S., Johnson, B., Johnson, C., Jones, A., Jones, C., Mann, G., Milton, S., Rumbold, H., Sellar, A., Ujiie, M., Whitall, M., Williams, K., and Zerroukat, M.:

Atmospheric
Chemistry
and Physics
Discussions
Open Access
EGU

The Met Office Unified Model Global Atmosphere 7.0/7.1 and JULES Global Land 7.0 configurations, Geosci. Model Dev., 12, 1909–1963, https://doi.org/10.5194/gmd-12-1909-2019, 2019.

Weast, R.C.: CRC Handbook of Chemistry and Physics, 1971-1972: A Ready Reference Book of Chemical and Physical Data, 1180   52nd ed., 1971.

West, R. E. L., Stier, P., Jones, A., Johnson, C. E., Mann, G. W., Bellouin, N., Partridge, D. G., and Kipling, Z.: The importance of vertical velocity variability for estimates of the in direct aerosol effects, Atmos. Chem. Phys., 14, 6369–6393, https://doi.org/10.5194/acp-14-6369-2014, 2014.

1185

Wexler, A. S. and Seinfeld, J. H.: The distribution of ammonium salts among a size and composition dispersed aerosol, Atmos. Environ., 24A, 1231–1246, 1990.

Wilson, D. R. and Ballard, S. P.: A microphysically based precipitation scheme for the UK Meteorological Office Unified 1190   Model, Q. J. Roy. Meteorol. Soc., 125, 1607–1636, https://doi.org/10.1002/qj.49712555707, 1999.

Wilson, D. R., Bushell, A. C., Kerr-Munslow, A. M., Price, J. D., and Morcrette, C. J.: PC2: A prognostic cloud fraction and condensation scheme. I: Scheme description, Q. J. Roy. Meteorol. Soc., 134, 2093–2107, https://doi.org/10.1002/qj.333, 2008

1195   Womack, C. C., McDuffie, E. E., Edwards, P. M., Bares, R., Gouw, J. A. A., Docherty, K. S., Dubé, W. P., Fibiger, D. L., Franchin, A., Gilman, J. B., Goldberger, L., Lee, B. H., Lin, J. C., Long, R., Middlebrook, A. M., Millet, D. B., Moravek, A., Murphy, J. G., Quinn, P. K., Riedel, T. P., Roberts, J. M., Thornton, J. A., Valin, L. C., Veres, P. R., Whitehill, A. R., Wild, R. J., Warneke, C., Yuan, B., Baasandorj, M., and Brown, S. S.: An Odd Oxygen Framework for Wintertime Ammonium Nitrate Aerosol Pollution in Urban Areas: NOx and VOC Control as Mitigation Strategies, Geophys. Res. Lett., 46, 4971– 1200   4979, https://doi.org/10.1029/2019GL082028, 2019.

Wood, N., Staniforth, A., White, A., Allen, T., Diamantakis, M., Gross, M., Melvin, T., Smith, C., Vosper, S., Zerroukat, M., and Thuburn, J.: An inherently mass-conserving semi-implicit semi-Lagrangian discretization of the deep-atmosphere global non-hydrostatic equations, Q. J. R. Meteorol. Soc., 140, 1505–1520, https://doi.org/10.1002/qj.2235, 2014.

1205

Woodward, S.: Modelling the atmospheric life cycle and radiative impact of mineral dust in the Hadley Centre climate model, J. Geophys. Res., 106, 18 155–18 166, 2001.

World Health Organisation (WHO): World health statistics 2020: monitoring health for the SDGs, sustainable development
1210 goals. Geneva: World Health Organization; 2020. Licence: CC BY-NC-SA 3.0 IGO, 2020.

Xu, L. and Penner, J. E.: Global simulations of nitrate and ammonium aerosols and their radiative effects, Atmos. Chem. Phys.,
12, 9479–9504, https://doi.org/10.5194/acp-12-9479- 2012, 2012.

1215 Xu, R., Tian, H., Pan, S., Prior, S. A., Feng, Y., Batchelor, W. D., Chen, J., and Yang, J.: Global ammonia emissions from
synthetic nitrogen fertilizer applications in agricultural systems: Empirical and process-based estimates and uncertainty, Glob.
Change Biol., 25, 314–326, https://doi.org/10.1111/gcb.14499, 2019.

Yienger, J. J., and Levy, H.: Empirical model of global soil-biogenic NO_x emissions, J. Geophys. Res., 100(D6), 11447,
1220 https://doi.org/10.1029/95JD00370, 1995.

Yool, A., Popova, E. E., and Anderson, T. R.: MEDUSA-2.0: an intermediate complexity biogeochemical model of the marine
carbon cycle for climate change and ocean acidification studies, Geosci. Model Dev., 6, 1767–1811, doi:10.5194/gmd-6-1767-
2013, 2013.

1225
Zaveri, R. A., Easter, R. C., Fast, J. D., and Peters, L. K.: Model for Simulating Aerosol Interactions and Chemistry (MOSAIC),
J. Geophys. Res., 113, D13204, doi:10.1029/2007JD008782., 2007.

Zerroukat, M. and Allen, T.: On the monotonic and conservative transport on overset/Yin-Yang grids, J. Comput. Phys., 302,
1230 285–299, https://doi.org/10.1016/j.jcp.2015.09.006, 2015.

Zhong, Q., Shen, H., Yun, X., Chen, Y., Ren, Y., Xu, H., Shen, G., Du, W., Meng, J., Li, W., Ma, J., and Tao, S.: Global Sulfur
Dioxide   Emissions   and   the   Driving   Forces,   Environ.   Sci.   Technol.,   54,   6508−6517,
https://dx.doi.org/10.1021/acs.est.9b07696, 2020.

1235
Zhu, L., Henze, D. K., Bash, J. O., Cady-Pereira, K. E., Shephard, M. W., Luo, M., and Capps, S. L.: Sources and Impacts of
Atmospheric NH_3: Current Understanding and Frontiers for Modeling, Measurements, and Remote Sensing in North America,
Curr. Pollution Rep., 1, 95–116, DOI 10.1007/s40726-015-0010-4, 2015